AN INFRARED CENSUS OF DUST IN NEARBY GALAXIES WITH SPITZER (DUSTiNGS), I. OVERVIEW

Martha L. Boyer[1,2], Kristen B. W. McQuinn[3], Pauline Barmby[4], Alceste Z. Bonanos[5], Robert D. Gehrz[3],
Karl D. Gordon[6], M. A. T. Groenewegen[7], Eric Lagadec[8], Daniel Lennon[9], Massimo Marengo[10],
Margaret Meixner[6], Evan Skillman[3], G. C. Sloan[11], George Sonneborn[1], Jacco Th. van Loon[12],
Albert Zijlstra[13]

ABSTRACT

Nearby resolved dwarf galaxies provide excellent opportunities for studying the dust-producing late stages of stellar evolution over a wide range of metallicity ($-2.7 \lesssim$ [Fe/H] $\lesssim -1.0$). Here, we describe DUSTiNGS (DUST in Nearby Galaxies with *Spitzer*): a 3.6 and 4.5 μm post-cryogen *Spitzer Space Telescope* imaging survey of 50 dwarf galaxies within 1.5 Mpc that is designed to identify dust-producing Asymptotic Giant Branch (AGB) stars and massive stars. The survey includes 37 dwarf spheroidal, 8 dwarf irregular, and 5 transition-type galaxies. This near-complete sample allows for the building of statistics on these rare phases of stellar evolution over the full metallicity range. The photometry is >75% complete at the tip of the Red Giant Branch for all targeted galaxies, with the exception of the crowded inner regions of IC 10, NGC 185, and NGC 147. This photometric depth ensures that the majority of the dust-producing stars, including the thermally-pulsing AGB stars, are detected in each galaxy. The images map each galaxy to at least twice the half-light radius to ensure that the entire evolved star population is included and to facilitate the statistical subtraction of background and foreground contamination, which is severe at these wavelengths. In this overview, we describe the survey, the data products, and preliminary results. We show evidence for the presence of dust-producing AGB stars in 8 of the targeted galaxies, with metallicities as low as [Fe/H] $= -1.9$, suggesting that dust production occurs even at low metallicity.

1. INTRODUCTION

1.1. *Dust Production by Evolved Stars*

Intermediate-mass ($1 M_\odot \lesssim M \lesssim 8 M_\odot$) and massive ($\gtrsim 8 M_\odot$) evolved stars are drivers of galaxy chemical enrichment and evolution via the return of significant amounts of gas and dust to the interstellar medium (ISM). This stellar mass loss also drives the subsequent evolution of the stars themselves. However, post-main sequence stellar evolution is poorly understood, especially

[1] Observational Cosmology Lab, Code 665, NASA Goddard Space Flight Center, Greenbelt, MD 20771 USA; martha.boyer@nasa.gov
[2] Oak Ridge Associated Universities (ORAU), Oak Ridge, TN 37831 USA
[3] Minnesota Institute for Astrophysics, School of Physics and Astronomy, 116 Church Street SE, University of Minnesota, Minneapolis, MN 55455 USA
[4] Department of Physics & Astronomy, University of Western Ontario, London, ON, N6A 3K7, Canada
[5] IAASARS, National Observatory of Athens, GR-15236 Penteli, Greece
[6] STScI, 3700 San Martin Drive, Baltimore, MD 21218 USA
[7] Royal Observatory of Belgium, Ringlaan 3, B-1180 Brussels, Belgium
[8] Laboratoire Lagrange, UMR7293, Univ. Nice Sophia-Antipolis, CNRS, Observatoire de la Côte d'Azur, 06300 Nice, France
[9] ESA - European Space Astronomy Centre, Apdo. de Correo 78, 28691 Villanueva de la Cañada, Madrid, Spain
[10] Department of Physics and Astronomy, Iowa State University, Ames, IA 50011, USA
[11] Astronomy Department, Cornell University, Ithaca, NY 14853-6801, USA
[12] Astrophysics Group, Lennard-Jones Laboratories, Keele University, Staffordshire ST5 5BG, UK
[13] Jodrell Bank Centre for Astrophysics, Alan Turing Building, University of Manchester, M13 9PL, UK

in the short-lived dust-producing phases. And it is unclear how the galactic environment (especially metallicity) affects stellar dust production and evolution. DUST in Nearby Galaxies with *Spitzer* (DUSTiNGS) is an infrared (IR) survey of 50 dwarf galaxies in and around the Local Group designed to detect evolved stars in the dust-producing phase.

Massive dusty evolved stars such as luminous blue variables, Wolf-Rayet stars, red supergiants, and supergiant B[e] stars are prolific dust producers (Smith 2014; Bonanos et al. 2010; Kastner et al. 2006; Voors et al. 2000; Smith et al. 2003), though it is uncertain how much, if any, dust will survive the subsequent supernova (SN) explosion. The role of episodic mass loss, which is often accompanied by dust production, in the evolution of massive stars remains an open question. The inferred presence of pre-existing circumstellar material around several core-collapse SNe (Smith et al. 2007) suggests that mass loss plays an important part in stellar evolution. The DUSTiNGS survey includes a large sample of nearby dwarf galaxies to increase the known sample of these short-lived stars over a wide range of stellar masses and metallicities.

Intermediate-mass Asymptotic Giant Branch (AGB) stars condense dust from material formed in situ and may be a major source of interstellar dust (Gehrz 1989) as inferred, for example, by the AGB origin of a large fraction of presolar grains found in meteorites (e.g., Gail et al. 2009). Several works have shown that a small population of very dusty AGB stars dominate the AGB dust production in the Magellanic Clouds at a given time (Srinivasan et al. 2009; Boyer et al. 2012; Riebel et al. 2012; Zhukovska & Henning 2013; Schneider et al. 2014).

These stars (sometimes called "extreme" AGB stars — or x-AGB stars) are optically obscured, and are generally selected via their red colors ($[3.6] - [8] > 3$ mag; see Section 6.1.2). They comprise $\lesssim 5\%$ of the AGB population, but produce more than 3/4 of the AGB dust. Through spectral energy distribution modeling, Riebel et al. (2012) find that most of these stars in the Large Magellanic Cloud are carbon rich. Carbon stars form easily in metal-poor environments because of a low initial oxygen abundance in the circumstellar envelope and hence more free carbon after the formation of C/O (e.g., Groenewegen & de Jong 1993). It follows that carbon stars may also dominate the dust production in the more metal-poor dwarf galaxies.

Nevertheless, it is still unclear how much AGB dust survives the harsh environment of the ISM produced by SN shocks (e.g., Jones & Nuth 2011). Recent *Spitzer* observations of the Small and Large Magellanic Clouds (SMC/LMC) by the Surveying the Agents of Galaxy Evolution program (SAGE; Meixner et al. 2006; Gordon et al. 2011) produced a complete census of AGB stars in those galaxies. Estimates of the total dust input compared with other known dust sources (i.e., supernovae ejecta) indicate that AGB stars may be the dominant source of stellar-produced dust grains (Matsuura et al. 2009; Boyer et al. 2012; Riebel et al. 2012; Zhukovska & Henning 2013; Schneider et al. 2014). These works also concluded that, despite their efficient dust production, AGB stars can account for only a fraction of the ISM dust mass in the SMC and LMC. However, a revised measurement of the SMC and LMC ISM dust masses using *Herschel Space Observatory* data is significantly smaller than previously estimated with *Spitzer* data (Gordon 2014), indicating that AGB stars may in fact be a dominant dust source in these galaxies.

1.2. *The Metallicity Dependence of Dust Production*

For more metal-poor populations, the metallicity dependence of dust production by AGB stars remains unclear. Some AGB stellar evolution models suggest that dust production easily occurs at very low metallicity because carbon stars create carbon in situ (e.g., Karakas & Lattanzio 2007; Mattsson et al. 2008; Wachter et al. 2008). Other models suggest that at very low metallicity ($[Fe/H] \lesssim -2$), AGB stars contribute little dust and thus provide a negligible contribution to the total dust budget of high-redshift galaxies (L. Mattsson, in preparation).

The effect of the metallicity on dust production likely differs for oxygen-rich and carbon-rich AGB stars because carbon stars create their own carbon. Photometric surveys of metal-poor globular clusters show modest dust-production by low-mass oxygen-rich AGB stars (Boyer et al. 2009a; McDonald et al. 2011b,a) down to $[Fe/H] \approx -1.7$. Infrared spectroscopy of O-rich AGB stars in the Magellanic Clouds and globular clusters reveals trends consistent with reduced dust production at lower metallicities, as expected due to reduced amounts of the oxygen needed to make silicate dust, but these studies are not conclusive (Sloan et al. 2008; Groenewegen et al. 2009; Sloan et al. 2010).

In carbon stars, some works suggest there is no metallicity dependence on dust formation (e.g., Groenewegen et al. 2007), while some do find hints of such a dependence at $[Fe/H] \lesssim -1$ (van Loon et al. 2008; Sloan
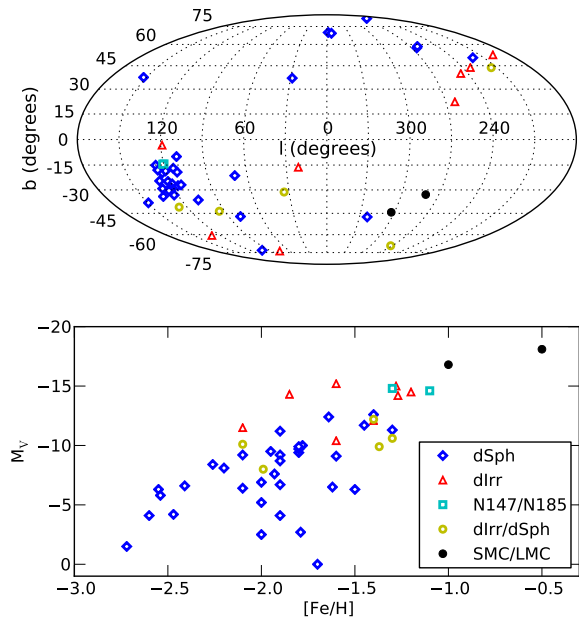

Figure 1. DUSTiNGS targets with properties from Table 1. *Upper panel:* Distribution of target galaxies in Galactic coordinates. Note there are few targets near the Galactic Plane/Bulge, limiting the effects of foreground extinction and contamination (Sections 5.2 and 5.3). The cluster of dSph galaxies near $l = 120°$ and $b = 20°$ is the Andromeda group. *Lower panel:* Distribution of target galaxies in absolute V-band magnitude (M_V) and metallicity ($[Fe/H]$). The Small and Large Magellanic Clouds (SMC/LMC) are shown for comparison.

et al. 2012). However, this latter group includes only two C stars in the Sculptor dwarf and three in Leo I ($[Fe/H] = -1.68$ and -1.43, respectively; McConnachie 2012). Larger samples at low metallicities are clearly needed.

The DUSTiNGS survey aims to build statistics of the short-lived dust-producing phase at low metallicity for constraining stellar evolution and dust production models. Here, we present an overview of the survey, which greatly extends the baseline in age and metallicity over previous observations (Table 1, Fig. 1), and provides a near-complete census of galaxies within 1.5 Mpc at 3.6 and 4.5 μm. The purpose of this overview is to describe the DUSTiNGS targets (Section 2), the observations and survey design (Section 3), and the data products (Sections 4 and 5). We also estimate the AGB population size (Section 6). Forthcoming papers will describe additional scientific results in detail; in Boyer et al. (2014, hereafter Paper II), we identify individual x-AGB star candidates via their pulsation.

2. THE TARGETS

2.1. *Nearby Dwarf Galaxies*

We describe the DUSTiNGS targets and their properties in Table 1 and Figure 1. Dwarf galaxies are the most prevalent morphological type of galaxy and may be the building blocks of larger galactic systems (Tosi 2003). Additionally, nearby dwarfs present a complete suite of galactic environments (e.g., metallicity and star formation history; Mateo 1998; McConnachie 2012) that is perfect for studying the connection between stellar

Table 1
Adopted Target Parameters

Galaxy	R.A. (J2000)	Dec (J2000)	$(m-M)_0$ (mag)	M_V (mag)	$12 + \log(O/H)$	[Fe/H]	r_h (′)	References
– Dwarf Spheroidals (dSph)								
And XVIII	00 02 14.5	+45 05 20	25.66 ± 0.13	-9.7 ± 0.1	$\cdots$	-1.80 ± 0.10	0.92 ± 0.06	1
And XX	00 07 30.7	+35 07 56	$24.35^{+0.12}_{-0.15}$	$-6.3^{+1.1}_{-0.8}$	$\cdots$	-1.50 ± 0.10	0.53 ± 0.14	1,2
And XIX	00 19 32.1	+35 02 37	$24.57^{+0.08}_{-0.36}$	-9.2 ± 0.6	$\cdots$	-1.90 ± 0.10	6.20 ± 0.10	1,2
Cetus	00 26 11.0	-11 02 40	24.39 ± 0.07	-11.2 ± 0.2	$\cdots$	-1.90 ± 0.10	3.20 ± 0.10	1
NGC 147	00 33 12.1	+48 30 32	24.15 ± 0.09	-14.6 ± 0.1	$\cdots$	-1.10 ± 0.10	3.17	1
And III	00 35 33.8	+36 29 52	24.37 ± 0.07	-10.0 ± 0.3	$\cdots$	-1.78 ± 0.04	2.20 ± 0.20	1
And XVII	00 37 07.0	+44 19 20	24.50 ± 0.10	-8.7 ± 0.4	$\cdots$	-1.90 ± 0.20	1.24 ± 0.08	1
NGC 185	00 38 58.0	+48 20 15	23.95 ± 0.09	-14.8 ± 0.1	8.20 ± 0.20	-1.30 ± 0.10	2.55	1,3
And I	00 45 39.8	+38 02 28	24.36 ± 0.07	-11.7 ± 0.1	$\cdots$	-1.45 ± 0.04	3.10 ± 0.30	1
And XI	00 46 20.0	+33 48 05	$24.40^{+0.20}_{-0.50}$	-6.9 ± 1.3	$\cdots$	-2.00 ± 0.20	0.71 ± 0.03	1
And XII	00 47 27.0	+34 22 29	24.70 ± 0.30	-6.4 ± 1.2	$\cdots$	-2.10 ± 0.20	1.20 ± 0.20	1
And XIV	00 51 35.0	+29 41 49	24.33 ± 0.33	-8.4 ± 0.6	$\cdots$	-2.26 ± 0.05	1.70 ± 0.80	1
And XIII	00 51 51.0	+33 00 16	$24.40^{+0.33}_{-0.40}$	-6.7 ± 1.3	$\cdots$	-1.90 ± 0.20	0.78 ± 0.08	1,2
And IX	00 52 53.0	+43 11 45	$23.89^{+0.31}_{-0.08}$	-8.1 ± 1.1	$\cdots$	-2.20 ± 0.20	2.50 ± 0.10	1,2
And XVI	00 59 29.8	+32 22 36	23.60 ± 0.20	-9.2 ± 0.4	$\cdots$	-2.10 ± 0.20	0.89 ± 0.05	1
And X	01 06 33.7	+44 48 16	24.23 ± 0.21	-7.6 ± 1.0	$\cdots$	-1.93 ± 0.11	1.30 ± 0.10	1
And V	01 10 17.1	+47 37 41	24.44 ± 0.08	-9.1 ± 0.2	$\cdots$	-1.60 ± 0.30	1.40 ± 0.20	1
And XV	01 14 18.7	+38 07 03	24.00 ± 0.20	-9.4 ± 0.4	$\cdots$	-1.80 ± 0.20	1.21 ± 0.05	1
And II	01 16 29.8	+33 25 09	24.07 ± 0.06	-12.4 ± 0.2	$\cdots$	-1.64 ± 0.04	6.20 ± 0.20	1
And XXII	01 27 40.0	+28 05 25	$24.82^{+0.07}_{-0.31}$	-6.5 ± 0.8	$\cdots$	-1.62 ± 0.05	0.94 ± 0.10	1,4,5
Segue 2	02 19 16.0	+20 10 31	17.70 ± 0.10	-2.5 ± 0.3	$\cdots$	-2.00 ± 0.25	3.40 ± 0.20	1
UMa II	08 51 30.0	+63 07 48	17.50 ± 0.30	-4.2 ± 0.6	$\cdots$	-2.47 ± 0.06	16.0 ± 1.0	1
Segue 1	10 07 04.0	+16 04 55	16.80 ± 0.20	-1.5 ± 0.8	$\cdots$	-2.72 ± 0.40	$4.4^{+1.2}_{-0.6}$	1
Willman 1	10 49 21.0	+51 03 00	17.90 ± 0.40	-2.7 ± 0.8	$\cdots$	-2.10	2.30 ± 0.40	1
Leo V	11 31 09.6	+02 13 12	21.25 ± 0.12	-5.2 ± 0.4	$\cdots$	-2.00 ± 0.20	2.60 ± 0.60	1
Leo IV	11 32 57.0	-00 32 00	20.94 ± 0.09	-5.8 ± 0.4	$\cdots$	-2.54 ± 0.07	4.60 ± 0.80	1
Coma	12 26 59.0	+23 54 15	18.20 ± 0.20	-4.1 ± 0.5	$\cdots$	-2.60 ± 0.05	6.00 ± 0.60	1
CVn II	12 57 10.0	+34 19 15	21.02 ± 0.06	-4.9 ± 0.5	$\cdots$	-2.20 ± 0.05	1.60 ± 0.30	1
Bootes II	13 58 00.0	+12 51 00	18.10 ± 0.06	-2.7 ± 0.9	$\cdots$	-1.79 ± 0.05	4.20 ± 1.40	1
Bootes I	14 00 06.0	+14 30 00	19.11 ± 0.08	-6.3 ± 0.2	$\cdots$	-2.55 ± 0.11	12.6 ± 1.0	1
Hercules	16 31 02.0	+12 47 30	20.60 ± 0.20	-6.6 ± 0.4	$\cdots$	-2.41 ± 0.04	$8.6^{+1.8}_{-1.1}$	1
Segue 3†	21 21 31.1	+19 07 03	16.1 ± 0.1	-0.0 ± 0.8	$\cdots$	$-1.7^{+0.1}_{-0.3}$	0.47 ± 0.13	6
Tucana	22 41 49.6	-64 25 10	24.74 ± 0.12	-9.5 ± 0.2	$\cdots$	-1.95 ± 0.15	1.10 ± 0.20	1
Pisces II	22 58 31.0	+05 57 09	21.31 ± 0.18	-4.1 ± 0.4	$\cdots$	-1.90	1.10 ± 0.10	1,7
And VII	23 26 31.7	+50 40 33	24.41 ± 0.10	-12.6 ± 0.3	$\cdots$	-1.40 ± 0.30	3.50 ± 0.10	1
And VI	23 51 46.3	+24 34 57	24.47 ± 0.07	-11.3 ± 0.2	$\cdots$	-1.30 ± 0.14	2.30 ± 0.20	1
And XXI	23 54 47.7	+42 28 15	24.67 ± 0.13	-9.9 ± 0.6	$\cdots$	-1.80 ± 0.20	3.50 ± 0.30	1
– Dwarf Irregulars (dIrr)								
WLM	00 01 58.2	-15 27 39	24.95 ± 0.03	-14.2 ± 0.1	7.83 ± 0.06	-1.27 ± 0.04	7.78	1,8,9
IC 10	00 20 17.3	+59 18 14	24.27 ± 0.18	-15.0 ± 0.2	8.19 ± 0.15	-1.28	2.65	1,3,10
IC 1613	01 04 47.8	+02 07 04	24.39 ± 0.12	-15.2 ± 0.2	7.62 ± 0.05	-1.60 ± 0.20	6.81	1,8,11
Leo A	09 59 26.5	+30 44 47	24.51 ± 0.12	-12.1 ± 0.2	7.35 ± 0.06	-1.40 ± 0.20	2.15	1,8,9,12
Sextans B	10 00 00.1	+05 19 56	25.60 ± 0.03	-14.5 ± 0.2	7.53 ± 0.05	-1.6	1.06 ± 0.10	1,3,8,9
Antlia	10 04 04.1	-27 19 52	25.65 ± 0.10	-10.4 ± 0.2	$\cdots$	-1.60 ± 0.10	1.20 ± 0.12	1,13
Sextans A	10 11 00.8	-04 41 34	25.60 ± 0.03	-14.3 ± 0.1	7.54 ± 0.06	-1.85	2.47	1,8,9
Sag DIG	19 29 59.0	-17 40 41	25.35 ± 0.18	-11.5 ± 0.3	7.42 ± 0.30	-2.10 ± 0.20	0.91 ± 0.05	1,3,13
– Transition Dwarfs (dTrans or dIrr/dSph)								
LGS 3	01 03 55.0	+21 53 06	$23.96^{+0.10}_{-0.07}$	-10.1 ± 0.1	$\cdots$	-2.10 ± 0.22	2.10 ± 0.20	1,14
Phoenix	01 51 06.3	-44 26 41	23.09 ± 0.10	-9.9 ± 0.4	$\cdots$	-1.37 ± 0.20	3.76	1,15
Leo T	09 34 53.4	+17 03 05	23.10 ± 0.10	-8.0 ± 0.5	$\cdots$	-1.99 ± 0.05	0.99 ± 0.06	1
Aquarius	20 46 51.8	-12 50 53	25.15 ± 0.08	-10.6 ± 0.1	$\cdots$	-1.30 ± 0.20	1.47 ± 0.04	1,16
Pegasus	23 28 36.3	+14 44 35	24.82 ± 0.07	-12.2 ± 0.2	7.93 ± 0.13	-1.40 ± 0.20	2.10	1,8,9,16

References. — Most values from (1) McConnachie (2012), and references therein. Other references: (2) Watkins et al. (2013), (3) Mateo (1998), (4) Martin et al. (2009), (5) Chapman et al. (2013), (6) Fadely et al. (2011), (7) Sand et al. (2012), (8) Lee et al. (2006), (9) Tammann et al. (2011), (10) Kim et al. (2009), (11) Bernard et al. (2010), (12) Bellazzini et al. (2014), (13) Pimbblet & Couch (2012), (14) Miller et al. (2001), (15) Menzies et al. (2008), and (16) McConnachie et al. (2005).

Note. — The half-light radius (r_h) is the distance along the semimajor axis that contains half the light of the galaxy.

† Segue 3 is likely a stellar cluster (e.g., Belokurov et al. 2010).

populations and galaxy evolution. DUSTiNGS includes all dwarf galaxies within 1.5 Mpc that were known at the time of the observations and that lacked sufficient coverage with *Spitzer* (see below). The next nearest galaxy (d=1.7 Mpc) is beyond IRAC's ability to resolve stars. Following McConnachie (2012), we divide the nearby resolved dwarfs into dwarf spheroidals (dSphs), dwarf irregulars (dIrrs), and transition (dIrr/dSph, or dTrans) galaxies.

The dSphs typically have no detected neutral hydrogen and show no evidence of recent star formation (within the last 200 Myr). The dSph galaxies are thought to have had their star formation terminated either through an internal process such as a galactic wind (e.g., Dekel & Silk 1986), an external process such as an interaction with a more massive host galaxy (e.g., Mayer et al. 2001, 2006), or heating by the ultraviolet field associated with reionization (e.g., Babul & Rees 1992; Efstathiou 1992).

The dIrrs are gas rich and show evidence of H II regions that are sites of current massive star formation. The dTrans galaxies are typically gas rich, but show no evidence of current massive star formation through the presence of H II regions. The nature of transition galaxies is a matter of debate. Many dTrans galaxies are consistent with dIrr galaxies that are forming stars at such a low rate that the absence of H II regions is consistent with stochastic variations. However, some show evidence for reduced gas mass fractions and apparently lie between the dSphs and dIrrs in the morphology-density relationship (e.g., Skillman et al. 2003; Weisz et al. 2011).

Most of the DUSTiNGS galaxies are members of the Local Group (Mateo 1998; McConnachie 2012). Based on their heliocentric radial velocities, van den Bergh (1999) argues that Sextans A, Sextans B, and Antlia are not Local Group members, but instead belong to a subgroup with NGC 3109 that is expanding with the Hubble flow (van den Bergh 1999).

Of those known before our observations, we exclude fifteen galaxies within 1.5 Mpc from DUSTiNGS because of existing *Spitzer* observations. Nine of the most nearby dSph galaxies were observed in cycle 5 using a similar observing strategy to the one employed here (P.I.: P. Barmby, PID 50134: CVn I, Draco, Fornax, Leo I, Leo II, Sculptor, Sextans, UMi, and UMa I). Carina, NGC 3109, NGC 6822, and NGC 205 were also covered by several *Spitzer* programs (PIDs: 128, 159, 3126, 3400, 20469, 40204, 61001, 70062). CMa and Sgr dSph are too large on the sky for efficient *Spitzer* imaging. Because they are also nearby (7 and 26 kpc, respectively), the Wide-Field Survey Explorer (WISE; Wright et al. 2010) all-sky IR survey is sufficiently sensitive to detect a large fraction of the dust-producing stars.

2.2. *Expected Dusty Stellar Populations*

Galaxies with different morphological types are expected to host different sized AGB and massive star populations based on both the typical mass scales and recent star formation histories. For example, dIrrs are typically more massive than the dSphs in the Local Group, so they should have a larger population of dusty stars. However, the level of recent star formation activity plays a significant role in determining the number of these stars per unit stellar mass of a galaxy. An intermediate-mass star enters the AGB stage of stellar evolution between
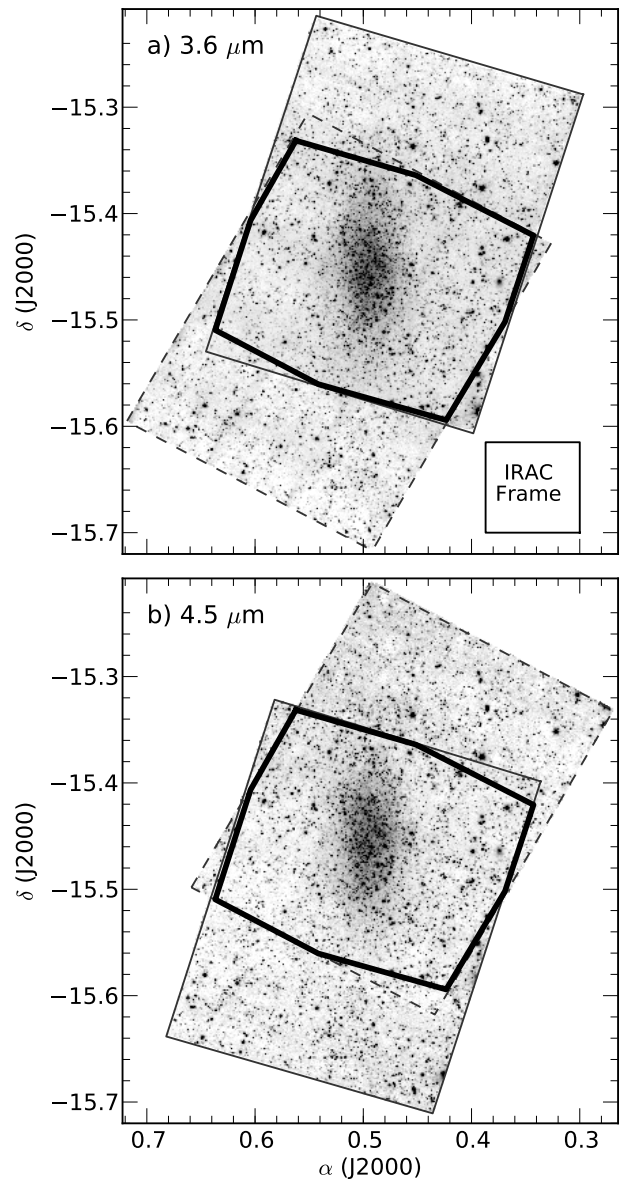

Figure 2. DUSTiNGS mapping strategy. *a)* 3.6 μm coadded mosaic for WLM. The solid thin line outlines the epoch 1 coverage and the dashed line outlines the epoch 2 coverage. The thick black line marks the coverage for all wavelengths and epochs, listed in Table 2. *b)* Same, for 4.5 μm. A similar mapping scheme was implemented for every galaxy. For WLM, the coverage is composed of a 3×4 grid of IRAC frames (5.′2×5.′2). Table 2 lists the grid size for each galaxy. The coverage listed in the last column of Table 2 includes only the area covered by all epochs and wavelengths.

about 100 Myr and 3 Gyr after formation depending on its initial mass (Marigo et al. 2013). Thus, galaxies with higher rates of star formation over these timescales will have larger populations of AGB stars and galaxies with more recent star formation will have massive stars. Because of the higher gas-rich content of dIrrs relative to dSphs, the two factors of stellar mass and recent star formation activity often compound one another.

However, differences do exist within each morphological type, with dSphs showing the greatest divergence in recent star formation activity (Weisz et al. 2014), adding some uncertainty to expectations on the AGB population

from this morphological type. Detailed studies of individual galaxies have shown that delayed onset of star formation is also possible. Both Leo A (Cole et al. 2007) and Leo T (Weisz et al. 2012) are examples of gas-rich galaxies that have formed the majority of their stars within the last 5-8 Gyr. Based on their overall lower mass, the number of AGB stars in each of these systems may be low even though a significant fraction of stellar mass in each galaxy was formed over the timescale of interest.

3. SURVEY DESIGN

The DUSTiNGS survey includes uniform 3.6 and 4.5-μm imaging of 50 nearby galaxies. These filters are particularly suited for identifying sources with warm dust (e.g., see the spectral energy distributions of dusty stars in Fig. 26 from Boyer et al. 2011). The observations are summarized in Table 2. DUSTiNGS uses the InfraRed Array Camera (IRAC; Fazio et al. 2004) onboard the *Spitzer Space Telescope* (Werner et al. 2004; Gehrz et al. 2007) during the post-cryogen phase. The spatial coverage extends to beyond the half-light radius (r_h; or the distance along the semimajor axis that contains half the visible light of the galaxy) at each wavelength for determining the level of foreground and background contaminating point sources. Each galaxy was observed at two epochs approximately 6 months apart to provide an additional diagnostic for identifying AGB stars, which are variable at these wavelengths (e.g., Le Bertre 1992, 1993; McQuinn et al. 2007; Vijh et al. 2009). The imaging footprint for WLM is shown in Figure 2 as an example of the DUSTiNGS mapping scheme.

Stellar evolution models (e.g., Bressan et al. 2012; Marigo et al. 2013) and previous studies at these wavelengths (e.g., Jackson et al. 2007a,b; Boyer et al. 2009b) show that the tip of the red giant branch (TRGB) is located at absolute 3.6-μm magnitude $-6.6 \lesssim M_{3.6} \lesssim -6$ mag. Thus, to ensure that the majority of thermally-pulsing (TP) AGB stars and dust-producing massive stars would be detected, the exposure times were chosen so that the 3-σ detection limit is at least one magnitude fainter than $M_{3.6} = -6$ mag. Together, the extended areal coverage and sensitivity enable the detection of most of the evolved stellar populations, thus significantly improving the statistics on these short-lived evolutionary phases. In particular, the DUSTiNGS sensitivity limit ensures the detection of nearly all of the x-AGB stars; in the Magellanic Clouds, >96% of the x-AGB stars (Section 6.1.2) are brighter than $M_{3.6} = -8$ mag.

For galaxies more distant than 400 kpc, we obtained 36 dithered frames with 30 s exposures at each map position (deep observations, $m_{3.6}^{5\sigma} \approx 20.5$ mag), one half of these frames were obtained in each epoch. Similarly, for galaxies with $130 < d < 400$ kpc, we obtained 5 dithered frames with 30 s exposures (medium, $m_{3.6}^{5\sigma} \approx 19.5$ mag) and for galaxies within 130 kpc, we obtained 5 dithered frames with 12 s exposures (shallow, $m_{3.6}^{5\sigma} \approx 18.5$ mag). In each case, we used the small cycling IRAC dither pattern with a median separation of 10.5 pixels to help eliminate imaging artifacts (the IRAC pixel size is $1''.22$). The map sizes and total exposure times ($t_{\exp}$) are listed in Table 2. The co-added, subsampled mosaics are available for download at the Mikulski Archive for Space Telescopes (MAST) and the InfraRed Science Archive (IRSA), and we show examples in Figures B1 and B2.
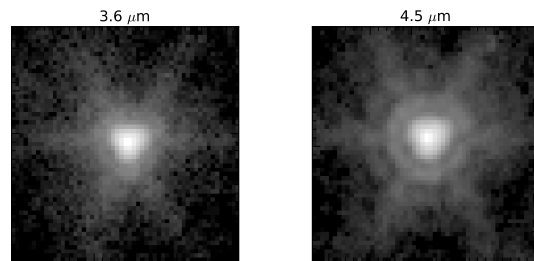

Figure 3. The subsampled ($0''.6$ pixels) point-spread functions, constructed using the data in DAOphot. The images are scaled logarithmically to show the wing structure.

4. POINT-SOURCE PHOTOMETRY

We describe below the photometry for the DUSTiNGS survey, including the photometric corrections, saturation, completeness, and crowding. The final photometric catalogs are available via MAST, IRSA, and VizieR.

4.1. PSF Photometry

Each galaxy in the DUSTiNGS survey was imaged over two epochs. We performed point-spread function (PSF) photometry separately for each epoch to aid in identification of variable stars, and also for a combined epoch to achieve the deepest photometry possible. Stars brighter than $\approx$16 mag (see below) were measured on the individual corrected Basic Calibrated Data (cBCD) frames from the *Spitzer* processing pipeline versions S18.18.0–S19.1.0 (depending on the date of observations), using a weighted mean to combine the measurements from each frame. The fainter magnitudes were recovered by performing PSF photometry on the co-added cBCD frames, with sub-sampled pixel sizes of $0''.6$. This two-step process is necessary to achieve accurate photometry for both the faint and bright sources. The photometry on the individual frames becomes unreliable at faint magnitudes due to the Eddington bias (Eddington 1913). This effect causes stars to appear too bright when approaching the detection limit because the source is more likely to be detected and measured if random fluctuations on the detector make a source brighter than its true flux. On the other hand, bright sources are very sensitive to the details of the PSF (Fig. 3), so their fluxes cannot be reliably measured on the mosaic where the PSF features are smeared due to rotation between the frames. Fainter sources are insensitive to these variations in the PSF and can thus be accurately measured from the mosaic, allowing for the maximum photometric depth.

All PSF photometry was carried out using DAOphot II and ALLSTAR (Stetson 1987), following a similar procedure to that used for the Galactic Plane Survey Extraordinaire (GLIMPSE; Benjamin et al. 2003) and SAGE (Meixner et al. 2006) programs (B. Babler, private communication). The PSF was constructed from the data itself, using the Pegasus dIrr images to select >10 bright, isolated stars with well-defined PSF wings (Fig. 3). For the photometry on the individual frames, we constructed the PSF using a Moffat function (Moffat 1969) with $\beta = 2.5$ for 3.6 μm and $\beta = 1.5$ for 4.5 μm where a larger β value approaches a Gaussian. The radius we used to fit the PSF to each source was $1''.6$–$2''.0$, or near the size of the FWHM. For the mosaic photometry, the PSF is different because co-adding the images

Table 2
Data & Observations

Galaxy	$\langle t_{\exp}\rangle$[a] (s)	$5\,\sigma$[a] (μJy)	Map[b] Size	AOR Key	Obs. Date (UTC)	AOR Key	Obs. Date (UTC)	Separation (days)	$N_{\rm ptsrc}$[c]	Coverage[d] (arcmin^2)
				— Epoch 1 —		— Epoch 2 —				
And I	1080	1.6	2×3	42307328	2011 Sep 08	42307584	2012 Mar 19	193.1	4640	85.6
And II	1080	1.6	2×3	42307840	2011 Sep 16	42308096	2012 Mar 15	181.3	4309	85.4
And III	1080	1.6	2×3	42308352	2011 Sep 24	42308608	2012 Mar 26	184.7	4043	85.9
And V	1080	1.6	2×3	42309376	2011 Sep 21	42309632	2012 Mar 27	188.0	4877	85.8
And VI	1080	1.6	2×3	42309888	2011 Sep 24	42310144	2012 Mar 09	167.8	4189	81.9
And VII	1080	1.6	2×3	42310400	2011 Aug 29	42310656	2012 Mar 20	203.4	6951	79.9
And IX	1080	1.6	2×3	42308864	2011 Sep 23	42309120	2012 Mar 27	186.3	4310	86.4
And X	1080	1.6	2×3	42310912	2011 Sep 19	42311168	2012 Mar 17	180.3	4826	83.3
And XI	1080	1.6	2×3	42311424	2011 Sep 08	42311680	2012 Mar 26	200.4	3200	83.9
And XII	1080	1.6	2×3	42311936	2011 Sep 24	42312192	2012 Mar 27	185.7	3739	86.1
And XIII	1080	1.6	2×3	42312448	2011 Sep 21	42312704	2012 Mar 27	188.4	3469	86.4
And XIV	1080	1.6	2×3	42312960	2011 Sep 19	42313216	2012 Mar 21	183.9	3211	86.0
And XV	1080	1.6	2×3	42313984	2011 Sep 19	42314240	2012 Mar 16	178.9	3794	84.5
And XVI	1080	1.6	2×3	42314496	2011 Sep 16	42314752	2012 Mar 21	187.3	3164	86.5
And XVII	1080	1.6	2×3	42315008	2011 Sep 23	42315264	2012 Mar 27	186.1	4736	86.2
And XVIII	1080	1.6	2×3	42315520	2011 Sep 06	42315776	2012 Mar 17	193.3	4297	85.2
And XIX	1080	1.6	2×3	42313472	2011 Sep 24	42313728	2012 Mar 17	175.6	3824	83.2
And XX	1080	1.6	2×3	42316032	2011 Aug 29	42316288	2012 Mar 18	201.7	2992	82.8
And XXI	1080	1.6	2×3	42329856	2011 Sep 23	42330112	2012 Mar 19	178.2	4505	82.8
And XXII	1080	1.6	2×3	42330368	2011 Sep 16	42330624	2012 Mar 15	181.2	3121	85.6
Antlia	1080	1.6	2×3	42316544	2011 Jun 28	42316800	2012 Feb 03	219.6	3666	76.6
Aquarius	1080	1.6	2×3	42319616	2011 Jun 22	42319872	2012 Jan 06	197.7	3072	86.2
Bootes I	60	9.1	4×5	42317056	2011 Sep 06	42317312	2012 Mar 13	189.2	3249	354.9
Bootes II	60	9.1	2×3	42317568	2011 Aug 28	42317824	2012 Mar 13	198.3	850	79.5
Cetus	1080	1.6	2×3	42318592	2011 Sep 17	42318848	2012 Feb 03	139.7	4041	79.8
Coma	60	9.1	3×4	42319104	2011 Jul 18	42319360	2012 Mar 13	239.7	1673	168.8
CVn II	150	4.4	2×3	42318080	2011 Jul 26	42318336	2012 Mar 13	231.4	2037	70.6
Hercules Dw	150	4.4	3×4	42320640	2011 Sep 20	42320896	2012 Apr 24	216.3	5434	174.2
IC 10	1080	1.6	3×4	42321152	2011 Sep 24	42321408	2012 Apr 04	193.1	48057	195.9
IC 1613	1080	1.6	4×5	42321664	2011 Sep 21	42321920	2012 Feb 20	153.2	23538	356.3
Leo A	1080	1.6	2×3	42322944	2012 Jan 09	42322688	2012 Jun 21	164.0	3680	83.1
Leo IV	150	4.4	2×3	42323200	2011 Jul 18	42323456	2012 Feb 15	212.4	1462	79.9
Leo T	1080	1.6	2×3	42323968	2012 Jan 08	42323712	2012 Jun 21	165.5	3394	86.1
Leo V	150	4.4	2×3	42331392	2011 Jul 17	42331648	2012 Feb 15	213.4	1470	80.1
LGS 3	1080	1.6	2×3	42322176	2011 Sep 21	42322432	2012 Mar 19	180.4	2558	85.9
NGC 147	1080	1.6	3×4	42324224	2011 Sep 23	42324480	2012 Mar 30	188.8	33748	201.3
NGC 185	1080	1.6	3×4	42324736	2011 Sep 19	42324992	2012 Apr 04	198.0	32021	192.5
Pegasus	1080	1.6	3×4	42320128	2011 Sep 17	42320384	2012 Jan 23	127.5	10688	179.8
Phoenix	1080	1.6	3×4	42325408	2011 Sep 09	42325504	2012 Jan 19	131.9	9474	167.2
Pisces II	150	4.4	2×3	42331904	2011 Aug 02	42332160	2012 Jan 12	163.6	1205	77.9
Sag DIG	1080	1.6	2×3	42326016	2011 Nov 20	42325760	2012 Jun 10	202.3	7102	85.8
Segue 1	60	9.1	2×3	42326528	2012 Feb 01	42326272	2012 Jun 23	142.7	718	79.7
Segue 2	60	9.1	2×3	42330880	2011 Sep 23	42331136	2012 Mar 15	174.1	598	79.8
Segue 3	60	9.1	2×3	42332416	2011 Jul 18	42332672	2012 Jan 02	167.7	1048	75.1
Sextans A	1080	1.6	3×4	42327040	2012 Feb 01	42326784	2012 Jul 19	168.9	8809	196.8
Sextans B	1080	1.6	3×4	42327552	2012 Feb 01	42327296	2012 Jun 25	145.4	9631	195.7
Tucana	1080	1.6	2×3	42327808	2011 Jun 19	42328064	2011 Nov 12	146.1	4374	72.5
UMa II	150	4.4	3×4	42328576	2012 Jan 02	42328320	2012 May 08	126.8	5056	163.1
Willman 1	150	4.4	2×3	42329600	2012 Jan 09	42329344	2012 Jun 05	148.4	2321	70.6
WLM	1080	1.6	3×4	42328832	2011 Sep 10	42329088	2012 Feb 01	144.0	12109	185.5

[a] The reported total exposure time per pixel and sensitivity are that of the combined epochs 1 and 2.
[b] Map size is the number of frames on each axis. A single IRAC frame is $5.'2 \times 5.'2$.
[c] Total number of reliable point sources (Section 4) within the spatial coverage listed in the last column.
[d] Total coverage in arcmin^2 that is included at all epochs and all wavelengths (e.g., marked by the thick black line in Fig. 2). This is smaller than the map size, which is the coverage at a single wavelength/epoch. This is the total coverage within which we can identify variable star candidates (Paper II). Galaxies with identical map sizes have slightly different total coverages owing to the rotation between the two epochs.

smears the point sources. To achieve the best match between the cBCD and mosaic photometry, we thus use a Moffat function ($\beta = 1.5$) and a Lorenz function for the 3.6 and 4.5 μm mosaic PSFs, respectively. The fitting radius was set to 3.2 pixels ($1.''9$).

In the final point-source catalog, the transition from cBCD to mosaic photometry occurs at a magnitude where the photometry from both is reliable and agrees to well within the photometric uncertainties. For the

medium and deep observations (150 s and 1080 s), this is at 16.5 mag and 15.7 mag for 3.6 and 4.5 μm, respectively. For the shallow observations (60 s), the transition is at 15.5 mag and 15.0 mag, respectively. We note that there may be discontinuities in the luminosity functions at the transition point.

4.2. Photometric Corrections

We applied several corrections to the photometry, as recommended by the Spitzer Science Center (SSC). First, the cBCD images were corrected for the pixel solid angle variation across the frame (at the level of 1%) and converted to data numbers for a robust measure of the photometric uncertainties.

Second, sources were corrected for the variation in the point-source flux across the array that is a result of the flat-fielding process (the Array-Location-Dependent correction). This effect can be as high as 10%, depending on the location of the source within the array. This correction is necessary for sources that are on the Rayleigh-Jeans tail within the IRAC filters, which includes most of the sources in our final catalogs. Here, we do not apply the Array-Location Dependent correction to point-sources that show a red color ($[3.6] - [4.5] > 0$ mag) with a $> 3\,\sigma$ significance.

Third, fluxes were adjusted by correcting for the location of the center of the point-source within a pixel since the quantum efficiency varies across each pixel (the Pixel Phase correction, up to 4%). Fourth, we applied a color correction for a 3000 K blackbody to the point-source fluxes, following the SSC's recommendation.

Following Fruchter & Hook (2002), we increased the measured flux uncertainties by a factor of 2 to account for correlated uncertainties between the pixels that arise from subsampling the mosaic. This correction was only applied to sources measured from the mosaics. Along with this uncertainty, the final photometric uncertainties include those reported by DAOphot and the calibration uncertainties listed by Reach et al. (2005) (Fig. 4).

The DUSTiNGS catalog includes magnitudes using the Vega-based zero points of 280.9 ± 4.1 Jy for 3.6 μm and 179.7 ± 2.6 Jy for 4.5 μm. The final photometry is well matched to that from WISE, which has filters similar to IRAC (3.4 and 4.6 μm, or W1 and W2). Agreement is within 0.02 mag down to the repeatability limit of the WISE photometry (≈ 14 mag). IRAC point-source positions are accurate to $\approx 0''\!.5$.

4.3. Saturation

The saturation limits for 30 s frames are 10.84 mag and 10.35 mag for 3.6 and 4.5 μm, respectively. For 12 s frames, the saturation limits are 9.86 mag and 9.34 mag. For the galaxies with $(m - M)_0 > 23$ mag, saturation only occurs for stars $\gtrsim 2$ mag brighter than the classical AGB limit, which lies near $-10 > M_{3.6} > -11$ mag ($M_{\rm bol} = -7.1$ mag, derived for 3.6 μm using the models from Groenewegen 2006). This includes all of the dIrr and dTrans galaxies. Because these galaxies are more likely to show evidence of recent/ongoing star formation, they are more likely to include massive AGB stars which approach (and sometimes slightly exceed) the classical AGB limit.

The nearest galaxies with $(m - M)_0 < 22$ mag are all dSph galaxies with little to no ongoing star formation. Any dust-producing stars in these galaxies are thus more likely to have low initial masses and luminosities near the TRGB. Nevertheless, saturation does occur at magnitudes fainter than the classical AGB limit for 9 galaxies (those within the shaded regions in Fig. 5a,b): Bootes I, Bootes II, Coma, Hercules, Segue 1, Segue 2, Segue 3, UMa II, and Willman 1.
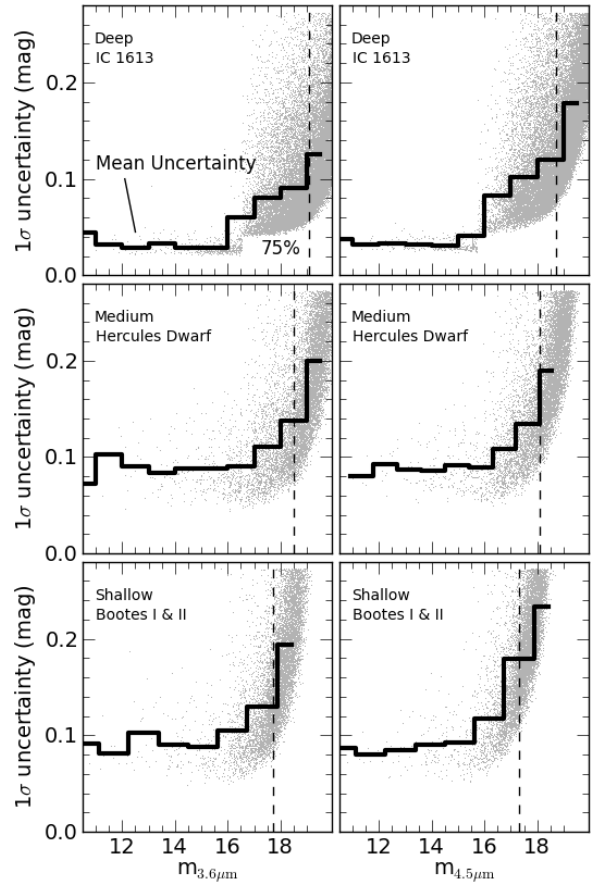

Figure 4. The photometric uncertainties from the Good-Source Catalog (GSC; Section 5) for galaxies observed at all three total exposure times (Table 2): IC 1613 (top), Hercules Dwarf (middle), and both Bootes galaxies (bottom). The Bootes I and II galaxies are combined to illustrate the photometric uncertainties because they both have few point sources. The discontinuities near 16 mag are caused by the use of photometry on the cBCD frames for brighter sources and on the co-added frames for faint sources. The 75% completeness level (Section 4.4) is shown as a dashed line in each panel. The histogram indicates the mean uncertainty at a given magnitude.

4.4. Photometric Completeness

To assess the repeatability of the photometry, we performed artificial star tests. For each galaxy and wavelength, we added 20 artificial stars of varying magnitudes to a 25 square arcmin region that excludes the galaxy center (crowding in the galaxy centers is discussed in Section 4.5). This was repeated 100 times, for a total of 2000 artificial stars. The magnitude distribution of the fake stars mimicked the real magnitude distribution (see Fig. 7). Table 3 lists the mean and the standard deviation in the resulting photometric completeness limits for galaxies unaffected by crowding (Section 4.5) and the completeness curves are shown in Figure 6.

The mean difference between the magnitudes of the added and recovered stars shows a small bias that increases with magnitude, but is $\lesssim 0.06$ mag and 0.02 mag for 3.6 and 4.5 μm, respectively, for stars brighter than
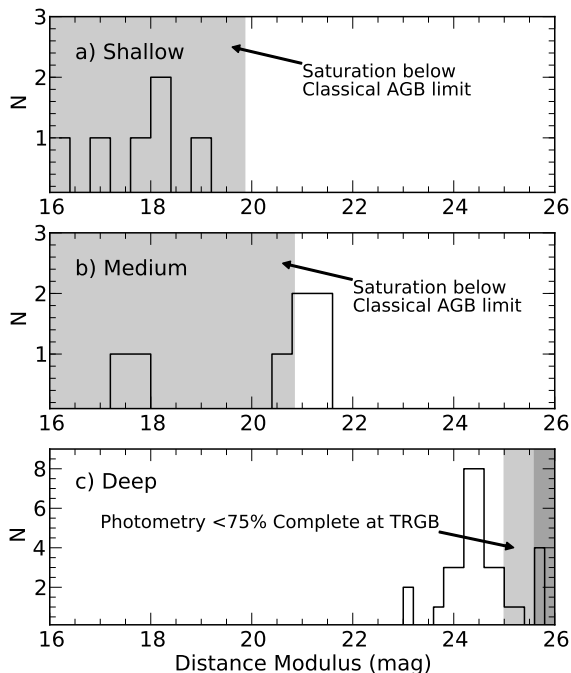
Figure 5. Number distribution of galaxies with saturation and photometric incompleteness for 3.6 μm. *a)* Galaxies with 60 s total integrations (12 s per frame). The shaded region marks the distance moduli where some stars fainter than the classical AGB limit ($M_{3.6} \gtrsim -10$ mag) will saturate. Bright (massive) stars in these galaxies are at risk of saturating. *b)* Galaxies with 150 s total integrations (30 s per frame). Those within the shaded region are at risk of saturating the brightest AGB stars. *c)* Galaxies with the deepest (1080 s) integrations (30 s per frame). AGB stars within these galaxies are not at risk of saturation. However, those with distance moduli within the light and dark shaded regions have <75% photometric completeness at $M_{3.6} = -6$ mag and -6.6 mag, respectively, which is the assumed range of the TRGB.

the 75% completeness limit (Fig. 7). For stars near 20$^{\text{th}}$ magnitude, the mean difference is $\lesssim 0.1$ mag. This bias is consistent with the effects of point-source crowding, which biases measurements towards brighter magnitudes and increases for faint sources. While only a few galaxies are affected by crowding above the TRGB (Section 4.5), all DUSTiNGS galaxies are affected by crowding at faint magnitudes. The final magnitudes are corrected for this bias.

For most galaxies, the photometry is better than 75% complete at $M_{3.6} = -6$ mag in each epoch, which is the approximate faint limit for the TRGB (Jackson et al. 2007a; Boyer et al. 2009b, 2011). At brighter magnitudes, the completeness rapidly increases (Fig. 6); we report the 75% limit throughout this work because it is representative of the completeness level near the TRGB for the most distant target galaxies. Six DUSTiNGS galaxies have <75% complete photometry at -6 mag (light shaded region of Fig. 5c) in a single epoch, though all six reach 75% completeness by -6.7 mag. In the photometry from the combined epochs, the completeness limit is approximately 0.5 mag fainter, resulting in near-complete photometry to the TRGB in all 50 galaxies.
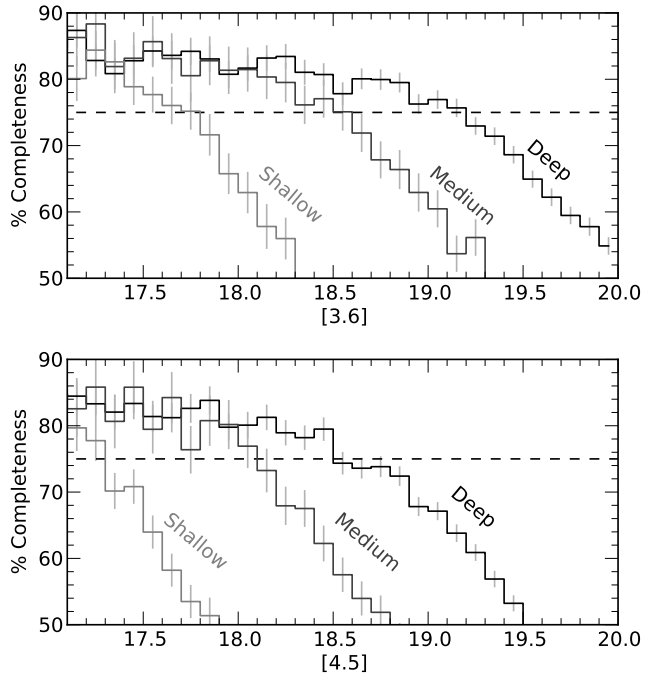
4.5. *Crowding*

Figure 6. Average completeness curves for the shallow, medium, and deep epoch 1 data. For the deeper, combined-epoch photometry, the completeness limits are approximately 0.5 mag fainter. The dashed line marks 75% completeness. These curves were derived for off regions (Section 4.4) and reflect only completeness due to sensitivity. These curves exclude galaxies that suffer from additional crowding; for those galaxies, the curves have similar shapes, shifted towards the brighter magnitudes listed in Table 3.
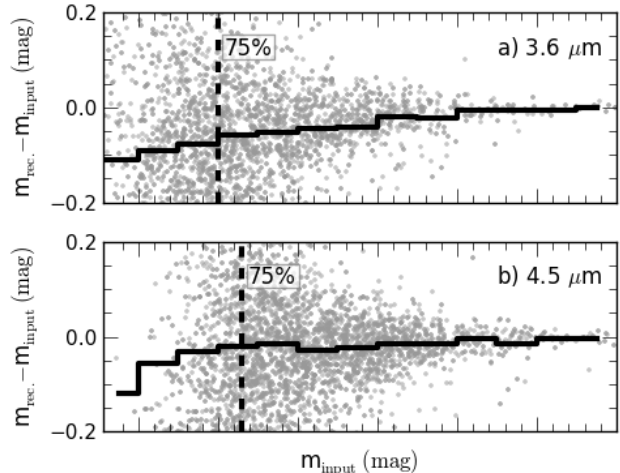

Figure 7. The difference between the input stellar magnitudes and the recovered stellar magnitudes from the artificial star tests. Three galaxies with $t_{\text{exp}} = 1080$ s are shown here. The 75% completeness limit is shown as a dashed line, and the solid black line shows the mean magnitude difference within 0.5 mag bins, excluding sources outside 3σ. The magnitudes in the published catalogs are corrected for the bias shown here.

Stellar crowding affects the photometric completeness both in the centers of dense galaxies (intrinsic) and for galaxies near the Galactic Plane, where foreground stars from the Milky Way increase the stellar density (extrinsic; Fig. 1).

We compute the photometric completeness as a func-

Table 3
75% Photometric Completeness Limits

$\langle t_{\exp} \rangle$ (s)	$3.6\,\mu$m (mag)	$4.5\,\mu$m (mag)
60	17.7 ± 0.2	17.3 ± 0.1
150	18.5 ± 0.2	18.1 ± 0.1
1080	19.1 ± 0.1	18.7 ± 0.2
– Galaxies affected by extrinsic crowding[a] –		
And VII	18.5 ± 0.2	18.5 ± 0.2
IC 10	17.7 ± 0.2	17.7 ± 0.2
NGC 147	18.2 ± 0.2	18.3 ± 0.2
NGC 185	18.6 ± 0.2	18.4 ± 0.2
Sag DIG	18.2 ± 0.2	17.9 ± 0.2

Note. — Completeness limits ($m_{75\%}$) were computed for the epoch 1 data. For the deeper, combined-epoch photometry, the completeness limit is approximately 0.5 mag fainter. The first three rows list the mean and standard deviation of the completeness limit for galaxies unaffected by crowding. All limits in this table were derived from a 25 arcmin^2 region away from the galaxy's center.

[a] All galaxies affected by extrinsic crowding have $\langle t_{\exp} \rangle = 1080$ s.

tion of radius to measure crowding from stars within the galaxies themselves. For most DUSTiNGS galaxies, internal crowding does not significantly affect the photometry. WLM and Sextans A show only slight crowding within 1′ of the their centers, affecting the photometric completeness by $\lesssim 0.2$ mag at 3.6 μm. Severe crowding is evident for IC 10, NGC 147, and NGC 185. Table 4 lists the radius where the photometry becomes 75% complete at absolute magnitudes of $M_{3.6} = -6$ and -8 mag, which are the limits used to identify AGB candidates in Section 6. IC 10 is the only galaxy for which the number of x-AGB (Section 1.2) candidates should be considered a lower limit.

All galaxies residing well above or below the Galactic Plane show similar completeness limits, but the 75% completeness limit rapidly increases in brightness as the distance from the Galactic Plane decreases. IC 10 and And VII have the smallest Galactic latitudes and are the most affected by foreground stars (Fig. 1). Sag DIG has a higher Galactic latitude but its longitude places it near the Galactic Bulge. The completeness limits for galaxies affected by extrinsic crowding are listed in Table 3.

5. DESCRIPTION OF THE CATALOG

The final Vega magnitudes of the high-quality point sources are reported in the DUSTiNGS "Good"-Source Catalog (GSC), which is described in Table 5 and is available to download from MAST, VizieR, and IRSA. To construct the GSC, we culled the full photometric catalogs using the sharpness (S) and chi (χ) parameters returned by DAOphot. To eliminate artifacts and extended objects, the sharpness value is restricted to $-0.3 < \langle S_{\lambda} \rangle < 0.3$. The χ parameter is a measure of the root-mean-square of the residuals and is restricted to $\langle \chi_{\lambda} \rangle < 5$ for sources measured from the cBCD frames and to $\langle \chi_{\lambda} \rangle < 2$ for those measured from the mosaics. In addition, the GSC includes only sources detected above the 4σ level and below the saturation limit and is restricted to sources that meet these criteria at both 3.6

Table 4
Intrinsic Crowding Limits

Galaxy	$m_{3.6}$ $= m_{75\%}$	$M_{3.6}$ $= -6\,$mag	$M_{3.6}$ $= -8\,$mag
IC 10	$R \approx 5'$	$\cdots$	$R \approx 1'$
NGC 147	$R \approx 4'$	$R \approx 4'$	All R
NGC 185	$R \approx 4'$	$R \approx 3'$	All R

Note. — The radii (R) where 75% completeness is reached for the given absolute magnitudes in galaxies that suffer from intrinsic crowding in their centers. Crowding was measured at radius intervals of 1′. Note that NGC 147 is elongated (ellipticity $\epsilon = 0.41 \pm 0.02$; McConnachie 2012), so photometry is complete at smaller radii along the minor axis.
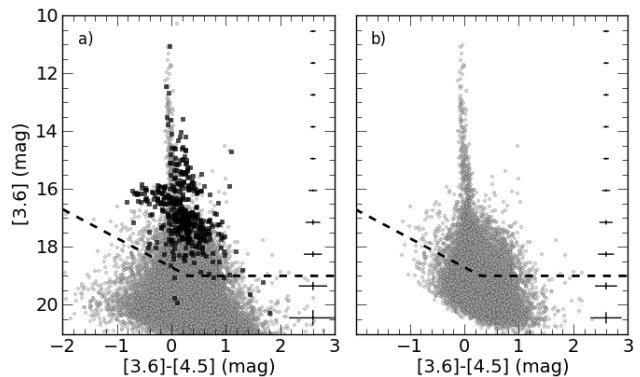

Figure 8. CMDs for And I showing *(a)* the full catalog and *(b):* the good-source catalog. In the full catalog, marginally resolved sources are marked by darker points (Section 5.1). The $[3.6] - [4.5]$ colors of extended sources can be artificially red or blue because fluxes may be extracted from the individual frames for one wavelength and from the mosaics for the other wavelength. The dashed line marks the 75% completeness limit. Mean photometric uncertainties are shown on the right of each panel.

Table 5
GSC Catalog Description

Column	Description
1	Galaxy Name
2	Point-source name; IAU convention
3–4	RA (h:m:s), Dec ($^{\circ}$: ′ : ″); J(2000)
5–8	3.6 μm mag and uncertainty for Epochs 1 & 2
9–12	4.5 μm mag and uncertainty for Epochs 1 & 2
13–14	DAOphot $S_{3.6}$ values for Epochs 1 & 2
15–16	DAOphot $S_{4.5}$ values for Epochs 1 & 2
17–18	DAOphot $\chi_{3.6}$ values for Epochs 1 & 2
18–19	DAOphot $\chi_{4.5}$ values for Epochs 1 & 2

Note. — The catalog is available for download via MAST, IRSA, and VizieR.

and 4.5 μm. Figure 8 shows an example color-magnitude diagram (CMD) of the full catalog compared with the GSC. The CMDs using the GSC for all targeted galaxies are presented in Figures A1 and A2.

5.1. *Marginally Resolved Extended Sources*

Extended sources that are unresolved or marginally resolved in the individual cBCD frames are more strongly resolved in the subsampled mosaic. There are several

sources measured from the cBCD frames that therefore meet the sharpness criteria for the GSC, but would
fail the same criteria if measured on the mosaic. Because these sources are extended, PSF photometry is
inappropriate and can result in large uncertainties; the
PSF-derived magnitude measured on the cBCD frames
can differ from that measured from on mosaic by 0.2
to 1 mag. For sources near the transition magnitude
where the individual-frame photometry and the mosaic
photometry were combined (Section 4.1), this results in
artificially blue or red colors (dark points in Fig. 8) if
stars were measured on the cBCD frames for one wavelength and on the mosaics for the other. These sources
are easily identified via a mean sharpness value created
by combining S_λ measured by DAOphot for all measured
channels and epochs from both the cBCD frames and
mosaics. This combined sharpness parameter is larger
for marginally resolved sources than for the true point-
sources at a given magnitude.

Removing these sources from the GSC significantly
decreases the contamination from background sources
brighter than ≈ 17 mag and allows for a more accurate
selection of stars belonging to the target galaxies. We do
not remove these sources from the full catalog because
we cannot rule out the possibility that they are indeed
galaxy members (e.g., star clusters). However, the PSF-
derived magnitudes for these sources are unreliable, so
we include only their positions in the full catalog and
recommend aperture photometry for accurate fluxes.

5.2. *Extinction*

We have not corrected for extinction in the photometric catalogs. With the exception of IC 10, all DUSTiNGS
galaxies show $E(B-V) < 0.2$ mag (McConnachie 2012).
At 3.6 and 4.5 μm, this level of extinction results in a
change in magnitude that is less than the photometric
uncertainties ($A_{3.6} < 0.03$ mag and $A_{4.5} < 0.02$ mag).

IC 10 has the smallest Galactic latitude, and thus the
highest level of extinction at $E(B-V) = 1.6$ mag. Correcting the IRAC magnitudes for extinction would result in a magnitude decrease of ~ 0.2 mag. However,
the change in color due to extinction is still well below the photometric uncertainties with $\Delta(m_{3.6}-m_{4.5}) <$
0.04 mag.

5.3. *Background and Foreground Contamination*

The DUSTiNGS field-of-view is large enough to provide a robust estimate of the foreground and background
sources. Figure 9c shows the epoch 1 CMD for Sextans A,
one of the more distant DUSTiNGS galaxies ($r_h = 2'.47$;
also see Fig. B2). To demonstrate a CMD with minimal contamination from nonmembers and a CMD that is
dominated by background and foreground, we also show
the CMDs of inner and outer regions of the Sextans A
coverage in Figure 9a,b. We show an estimate of the
foreground in panel d, simulated with the TRILEGAL
stellar population synthesis code (Girardi et al. 2005).
The difficulty in distinguishing between dusty stars with
$[3.6] - [4.5] > 0.1$ mag and $M_{3.6} < -8$ mag and unresolved background sources in the same color-magnitude
space (shaded region of Fig. 9) is clear when comparing panels $a)$ and $b)$. Less dusty member stars (with
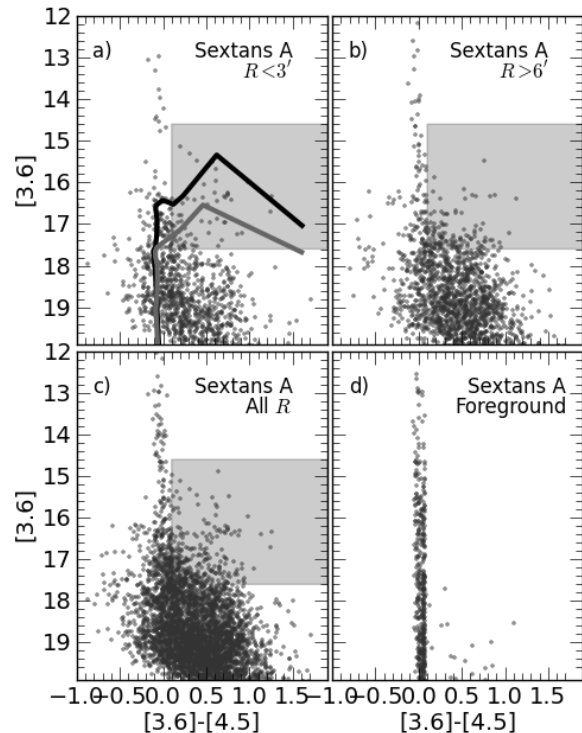$[3.6] - [4.5] \approx 0$ mag) are also difficult to identify due to

Figure 9. Epoch 1 CMD for Sextans A, showing $a)$ sources within
$3'$, $b)$ sources beyond $6'$, $c)$ the entire coverage, and $d)$ foreground
simulation for the full spatial coverage (Table 2) from TRILEGAL.
The shaded region shows the approximate location of x-AGB stars,
based on their position on the same CMD in the Magellanic Clouds
(Section 6.1.2; Blum et al. 2006; Bolatto et al. 2007; Boyer et al.
2011). The half-light radius for Sextans A is $2'.47$, with an ellipticity
of only 0.17 (Fig. B2; McConnachie 2012). In panel $a)$, the dark
and light solid lines are 400 Myr and 1 Gyr isochrones, respectively,
from Marigo et al. (2008).

confusion with both background and foreground sources.
Because AGB stars and some massive stars are variable,
the dual-epoch DUSTiNGS observations are crucial for
identifying individual member stars (Paper II).

In galaxies with a large intermediate-aged stellar population, a branch of x-AGB stars (Section 6.1.2) that
follows the isochrones shown in Figure 9a is easily identifiable in the CMD (Figs. A1 and A2). This feature
is clearly visible in only a handful of the DUSTiNGS
galaxies: IC 10, IC 1613, NGC 147, and NGC 185. Even
in other star-forming DUSTiNGS galaxies (e.g., WLM,
Sag DIG, Sextans A, Sextans B, and Pegasus dIrr), this
branch is not easily distinguished from background
sources.

5.4. *Luminosity Functions*

Most of the DUSTiNGS galaxies have smaller angular
sizes than the field-of-view (Table 1) and the recovered
photometry is therefore dominated by foreground and/or
background sources. We demonstrate this in Figure 10
for Cetus, Aquarius, and Sag DIG. Cetus is far from the
Galactic Plane ($b = -73°$; Fig. 1), so is dominated by
red background sources. This causes the 4.5 μm luminosity function to appear brighter than the 3.6 μm luminosity function. It also results in a sharp drop-off near
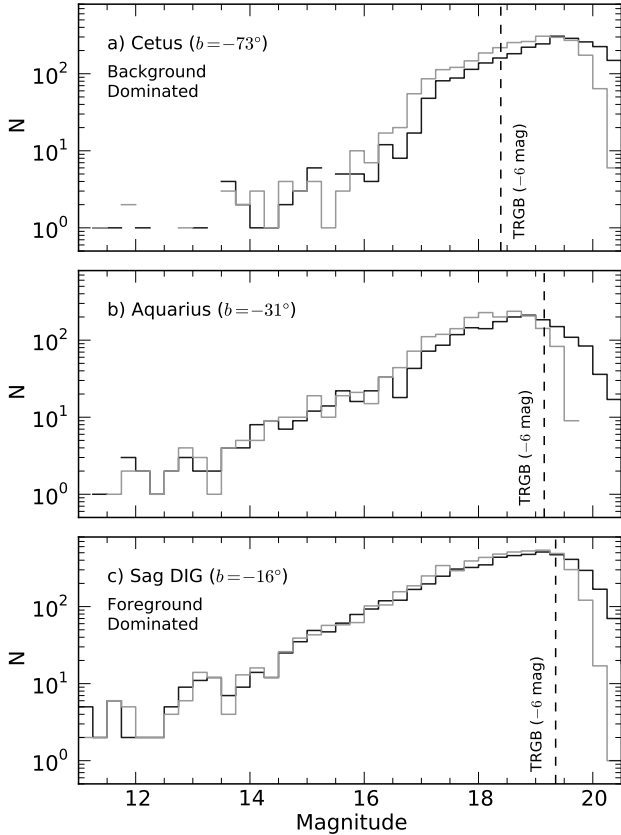
Figure 10. Luminosity functions for a) Cetus, b) Aquarius, and c) Sag DIG. The black and gray lines are the 3.6 µm and 4.5 µm luminosity functions, respectively. Because Cetus lies far from the Galactic Plane, its luminosity function is dominated by red background sources, mostly fainter than 17 mag. Sag DIG ($b = -16°$) is dominated by foreground from the Galactic Bulge. In all panels, the expected TRGB ($M_{[3.6]} \approx -6$ mag) is marked with a dashed line.
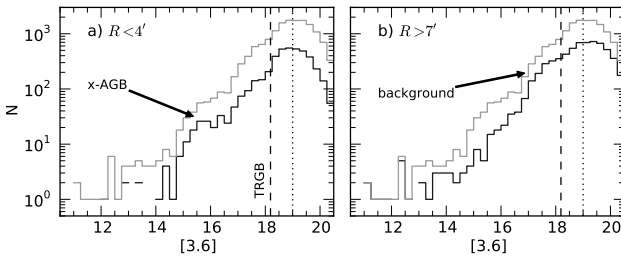

Figure 11. 3.6 µm luminosity function for IC 1613 for a) an on region ($r_h = 6'.8$), and b) an off region. The dusty AGB stars (x-AGB; Section 6.1.2) are clearly visible in the on region and missing in the off region. The TRGB measured by Jackson et al. (2007b) and Boyer et al. (2009b) is marked with a dashed line, and the 75% completeness limit is marked with a dotted line. The gray histogram shows the luminosity function for the entire field of view.

17 mag, because most of the brighter background galaxies have been eliminated from the GSC (Section 5.1). At the other extreme, Sag DIG is along a line-of-sight near the Galactic Bulge ($b = -16°$). Foreground therefore dominates its luminosity function and since these stars have colors near zero, the luminosity function is nearly the same at both wavelengths. Aquarius is at an intermediate latitude and shows the signatures of both

foreground and background sources.

In Figure 11, we show the 3.6 µm luminosity function for on and off regions towards IC 1613, which is known to harbor a large intermediate-aged stellar population (e.g., Skillman et al. 2014). At $R < 4'$, the TRGB and a feature attributed to x-AGB stars (Section 6.1.2) are visible. These same features are visible in other galaxies with large AGB populations. For $R > 7'$, a feature attributable to background sources is visible from $17 < m_{[3.6]} < 18$ mag.

6. THE IR STELLAR POPULATIONS

We cannot separate member stars from background/foreground sources with only the DUSTiNGS wavelengths. Therefore, we statistically subtract foreground and background sources to estimate the sizes of the TP-AGB (N_{TRGB}) and x-AGB (N_{xAGB}) populations. In Paper II, we use the 2-epoch variability information to identify a subset of individual AGB stars.

6.1. Stellar Classification

6.1.1. AGB Stars (N_{TRGB})

We classify all sources brighter than the TRGB as TP-AGB candidates, and assume that the TRGB lies at $M_{3.6} = -6$ mag. The TRGB is unknown for most of the DUSTiNGS galaxies, but Jackson et al. (2007a,b) and Boyer et al. (2009b) find that it is $-6.6 < M_{3.6} < -6$ mag for 8 of the DUSTiNGS dIrr galaxies. Using the Padova stellar evolution models (Marigo et al. 2008, 2013), Bruzual et al. (2013) created simple stellar population models of the Magellanic Clouds. They find that >90% of the thermally-pulsing (TP-)AGB stars are brighter than the TRGB (G. Bruzual 2013, private communication), so using the TRGB cutoff ensures that most of TP-AGB stars are included here. We apply no additional color cuts to the general TP-AGB classification.

The photometry is not 100% complete at the assumed TRGB for most of the DUSTiNGS galaxies. We therefore include a completeness-corrected value of N_{TRGB} in Table 6 (see below). We do not, however, correct for intrinsic crowding, which affects only the inner $1'$ of IC 10, NGC 147, and NGC 185.

The parameter N_{TRGB} includes AGB stars, massive young stars, and massive evolved stars. Without data at shorter wavelengths, it is impossible to know what fraction of N_{TRGB} is indeed AGB stars. In the Magellanic Clouds, AGB stars account for 38% (LMC) to 43% (SMC) of the stars brighter than -6 mag (derived from SAGE data after subtraction of foreground sources; Boyer et al. 2011). For galaxies with recent star formation (i.e., the dIrr galaxies and NGC 185 and NGC 147), we expect that the number of AGB candidates is $\gtrsim 0.3 N_{\mathrm{TRGB}}$, based on the LMC and SMC results. In the quiescent galaxies (i.e., most of the dSph galaxies), we can be confident that all, or nearly all, of N_{TRGB} are AGB candidates. Stars more massive than $M \gtrsim 8 \, M_\odot$ will not go through the AGB phase, so unless star formation has occurred in the last 50 Myr, there will not be contamination from massive stars in N_{TRGB}.

6.1.2. x-AGB Stars (N_{xAGB})

The x-AGB stars are a very dusty subset of the general TP-AGB population (N_{TRGB} includes N_{xAGB}). More

than 90% of TP-AGB stars with $[3.6] - [4.5] > 0.1$ mag and $M_{3.6} = -8$ mag in the Magellanic Clouds are classified as x-AGB stars by Blum et al. (2006) and Boyer et al. (2011), and we use the same criteria to classify them here. We emphasize that the x-AGB label is not synonymous with dust-producing, nor is it exclusive; TP-AGB stars with bluer colors may be producing dust, though at a smaller rate (Riebel et al. 2012; Boyer et al. 2012). This x-AGB star classification is based solely on the observed IR color, and it roughly corresponds to AGB sources that are in the superwind phase, when the mass-loss rate exceeds the nuclear-consumption rate and the dust-production rate can increase by more than a factor of 10.

For galaxies observed with the longest total exposure times ($t_{\rm exp} = 1080$ s), the magnitude uncertainties for x-AGB stars is $\lesssim 0.04$ mag (1σ; Fig. 4), so a color of $[3.6] - [4.5] = 0.1$ mag has a significance of $\gtrsim 2.5\sigma$. Therefore, the x-AGB class will include some sources that are not truly dusty and vice versa. For galaxies with shorter total exposure times ($t_{\rm exp} = 60$ s and 150 s), the photometric uncertainties are larger and lie around 0.1 mag. In these cases, any infrared excess will have less significance. However, none of the galaxies with medium and shallow total exposure times show evidence for *any* sources redder than $[3.6] - [4.5] = 0.1$ mag, AGB or otherwise (Table 6).

$N_{\rm xAGB}$ excludes most of the AGB stars with low mass-loss rates, massive red supergiant stars, and massive main-sequence stars. The result thus provides an estimate of the number of (mostly C-rich) x-AGB stars, with limited contamination from other source types (cf. Bonanos et al. 2010; Boyer et al. 2011; Sewiło et al. 2013).

We caution that the notation used for dusty AGB stars varies. For example, Gruendl et al. (2008) reserve the term "extreme AGB stars" for the rarest, dustiest stars with $[3.6] - [4.5] \gtrsim 3$ mag.

6.2. *Background/Foreground Source Subtraction*

Each DUSTiNGS galaxy was observed with a large field of view to assist in subtracting the contribution of background and foreground sources. To estimate $N_{\rm TRGB}$ and $N_{\rm xAGB}$, we first determine the distance from each galaxy center where the radial profile of point sources becomes flat and measure the density of sources with the relevant colors and magnitudes beyond this distance ($\Sigma_{\rm N}$). We then subtract $\Sigma_{\rm N} \times$ coverage area (Table 2) from the total number of point sources to obtain $N_{\rm TRGB}$ and $N_{\rm xAGB}$.

In regions where the stellar density is high, background galaxies are undetectable. In these regions, we subtract only the foreground sources, which we estimate for the position of each target galaxy using the TRILEGAL population synthesis code (Girardi et al. 2005, see Fig. 9). Table 6 lists the resulting AGB population sizes. The uncertainties in these numbers are derived from background-limited Poisson statistics. If the number of sources is below the 1.6σ limit, we quote 95% confidence upper limits.

Table 6 includes both the raw values of $N_{\rm TRGB}$ and $N_{\rm xAGB}$ and values that have been corrected for photometric completeness using each galaxy's completeness curve (Fig. 6 shows the mean completeness curve for each photometric depth). To make this correction, we first apply the completeness curve to the total number

of counts and to $\Sigma_{\rm N}$ individually, then compute $N_{\rm TRGB}$ and $N_{\rm xAGB}$ from those corrected values.

6.3. *Dust Production at Very Low Metallicity*

While most of the x-AGB stars in the DUSTiNGS sample are in the massive, more metal-rich galaxies (IC 10, NGC 147, NGC 185, and WLM), we find 166 ± 28 x-AGB stars at $[{\rm Fe/H}] \approx -1.6$ and 9 ± 4 at $[{\rm Fe/H}] \approx -1.9$ (Cetus). These are some of the most metal-poor dusty AGB stars known, and they are likely to be C-rich. AGB stars in the SMC with similar $[3.6] - [4.5]$ colors have an average dust-production rate of $\log(\dot{D}) = -8.7$ $[M_\odot/{\rm yr}]$ (Boyer et al. 2012).

For galaxies with $[{\rm Fe/H}] < -2$, we can quote only upper limits for the number of x-AGB stars. On the other hand, we do detect 1645 ± 240 AGB stars with less dust in these metal-poor galaxies (And XI, And XII, And XIV, And XVI, Hercules, Leo T, Sag DIG). In the SMC, AGB stars at these colors have dust-production rates of $-10.7 < \log(\dot{D}) < -10.1$ $[M_\odot/{\rm yr}]$. Because the x-AGB population sizes are detected statistically, we can say little about the properties of the individual stars (e.g., their distribution in color and luminosity and their dust-production rates). In Paper II, we identify a subset of the individual x-AGB stars and further describe their characteristics.

7. CONCLUSIONS

DUSTiNGS is a 3.6 and 4.5 μm photometric survey of 50 resolved dwarf galaxies within 1.5 Mpc designed to detect dusty evolved stars. The survey includes 37 dSph galaxies, 8 dIrr galaxies, and 5 dIrr/dSph transition-type galaxies. The large sample size allows for robust statistics on the short-lived, dust-producing phase. Each galaxy was observed over two epochs to aid in identifying variable AGB stars; Paper II presents the results of the variability analysis. Here, we describe the targets, the observing strategy, and the publicly-available data products.

For all galaxies, the photometry is >75% complete within the possible magnitude range of the TRGB with the exception of the inner regions of the most crowded galaxies: IC 10, NGC 147, and NGC 185. This completeness enables the detection of most of the AGB and massive evolved star populations. The photometric catalogs are publicly available at MAST, VizieR, and IRSA.

Because it is difficult to distinguish dusty evolved stars from unresolved background objects at these wavelengths, the DUSTiNGS survey imaged an area larger than the half-light radius of each galaxy to allow for statistical subtraction of foreground and background sources. We present here an estimate of the size of the stellar population brighter than the TRGB and the size of the dusty AGB star population. We find 1062 ± 103 "extreme" dusty AGB stars in 21 of the DUSTiNGS galaxies. For the remaining 29 DUSTiNGS galaxies we report 95% confidence upper limits.

Table 6
AGB Population Size

	— Raw Counts —		— Corrected —			— Raw Counts —		— Corrected —	
Galaxy	N_{TRGB}[a]	N_{xAGB}[b]	N_{TRGB}[a]	N_{xAGB}[b]	Galaxy	N_{TRGB}[a]	N_{xAGB}[b]	N_{TRGB}[a]	N_{xAGB}[b]
And I	168 ± 33	≤ 7	197 ± 36	≤ 8	Coma	≤ 3	0	≤ 3	0
And II	73 ± 31	9 ± 4	86 ± 34	11 ± 4	CVn II	≤ 5	0	≤ 5	0
And III	136 ± 31	≤ 6	163 ± 34	≤ 7	Hercules	20 ± 9	0	24 ± 10	0
And V	71 ± 39	≤ 8	77 ± 43	≤ 8	IC 10[†]	$11\,200 \pm 137$	516 ± 23	$16\,996 \pm 158$	597 ± 25
And VI	160 ± 30	≤ 6	190 ± 33	≤ 6	IC 1613	2224 ± 85	64 ± 10	2607 ± 91	67 ± 11
And VII	506 ± 48	≤ 10	628 ± 54	≤ 11	Leo A	53 ± 28	≤ 5	63 ± 31	≤ 5
And IX	≤ 44	≤ 3	≤ 47	≤ 3	Leo IV	≤ 6	0	≤ 6	0
And X	227 ± 35	≤ 6	266 ± 38	≤ 6	Leo T	32 ± 12	≤ 1	36 ± 13	≤ 1
And XI	95 ± 30	≤ 7	110 ± 33	≤ 7	Leo V	≤ 5	0	≤ 6	0
And XII	110 ± 36	≤ 9	132 ± 40	≤ 9	LGS 3	≤ 34	≤ 3	≤ 36	≤ 3
And XIII	119 ± 31	≤ 6	146 ± 34	≤ 6	NGC 147[†]	4646 ± 88	109 ± 12	6342 ± 100	124 ± 13
And XIV	50 ± 29	≤ 5	58 ± 31	≤ 5	NGC 185[†]	4119 ± 78	86 ± 10	5180 ± 86	99 ± 11
And XV	46 ± 26	≤ 4	55 ± 29	≤ 5	Pegasus	742 ± 54	≤ 11	882 ± 58	≤ 12
And XVI	40 ± 30	≤ 1	46 ± 21	≤ 1	Phoenix	61 ± 16	≤ 2	68 ± 17	≤ 3
And XVII	128 ± 38	≤ 9	150 ± 41	≤ 10	Pisces II	≤ 9	0	≤ 10	0
And XVIII	317 ± 53	≤ 24	406 ± 60	≤ 26	Sag DIG	829 ± 79	≤ 26	1239 ± 92	≤ 29
And XIX	≤ 62	≤ 9	≤ 67	≤ 9	Segue 1	≤ 1	0	≤ 1	0
And XX	130 ± 30	≤ 7	157 ± 33	≤ 8	Segue 2	≤ 2	0	≤ 3	0
And XXI	116 ± 39	≤ 10	135 ± 43	≤ 11	Segue 3	≤ 1	0	≤ 2	0
And XXII	99 ± 36	≤ 8	122 ± 40	≤ 9	Sextans A	965 ± 79	≤ 34	1230 ± 88	≤ 37
Antlia	204 ± 48	≤ 23	260 ± 54	≤ 25	Sextans B	1613 ± 75	77 ± 20	2118 ± 86	88 ± 22
Aquarius	205 ± 75	≤ 14	253 ± 53	≤ 15	Tucana	150 ± 35	≤ 6	183 ± 38	≤ 6
Bootes I	≤ 8	0	≤ 8	0	UMa II	≤ 2	0	≤ 2	0
Bootes II	0	0	0	0	Willman 1	0	0	0	0
Cetus	140 ± 29	7 ± 4	166 ± 31	9 ± 4	WLM	1764 ± 72	59 ± 12	2077 ± 78	67 ± 13

Note. — The size of the stellar population derived by subtracting the background and foreground contamination. Upper limits at 95% confidence are quoted when AGB stars are not detected above the level of background+foreground sources. The sources included here are confined to the spatial area covered by all epochs and wavelengths (Table 2). We report both the raw counts and the counts corrected for photometric completeness (Section 4.4).

[a] Stars that are brighter than $M_{3.6} = -6$ mag. Depending on the star-formation history of the galaxy, the total number of AGB stars can range from $0.3\,N_{\mathrm{TRGB}} - N_{\mathrm{TRGB}}$ (see text).

[b] xAGB stars are those brighter than $M_{3.6} = -8$ mag and redder than $[3.6] - [4.5] = 0.1$ mag.

[†] These galaxies are affected by intrinsic crowding in their centers (Table 4), so N_{TRGB} should be considered a lower limit in these cases. Crowding does not affect N_{xAGB} except within the central $\approx 1'$ region of IC 10. We have not corrected numbers in this table for intrinsic crowding.

REFERENCES

Babul, A. & Rees, M. J. 1992, MNRAS, 255, 346
Bellazzini, M., et al. 2014, A&A, 566, A44
Belokurov, V., et al. 2010, ApJ, 712, L103
Benjamin, R. A., et al. 2003, PASP, 115, 953
Bernard, E. J., et al. 2010, ApJ, 712, 1259
Blum, R. D., et al. 2006, AJ, 132, 2034
Bolatto, A. D., et al. 2007, ApJ, 655, 212
Bonanos, A. Z., et al. 2010, AJ, 140, 416
Boyer, M. L., et al. 2009a, ApJ, 705, 746
—. 2014, ApJ, submitted (Paper II)
—. 2009b, ApJ, 697, 1993
—. 2012, ApJ, 748, 40
—. 2011, AJ, 142, 103
Bressan, A., et al. 2012, MNRAS, 427, 127

Bruzual, G., et al. 2013, in IAU Symposium, Vol. 295, IAU Symposium, ed. D. Thomas, A. Pasquali, & I. Ferreras, 282–285
Chapman, S. C., et al. 2013, MNRAS, 430, 37
Cole, A. A., et al. 2007, ApJ, 659, L17
Dekel, A. & Silk, J. 1986, ApJ, 303, 39
Eddington, A. S. 1913, MNRAS, 73, 359
Efstathiou, G. 1992, MNRAS, 256, 43P
Fadely, R., et al. 2011, AJ, 142, 88
Fazio, G. G., et al. 2004, ApJS, 154, 10
Fruchter, A. S. & Hook, R. N. 2002, PASP, 114, 144
Gail, H.-P., et al. 2009, ApJ, 698, 1136
Gehrz, R. 1989, in IAU Symposium, Vol. 135, Interstellar Dust, ed. L. J. Allamandola & A. G. G. M. Tielens, 445
Gehrz, R. D., et al. 2007, Review of Scientific Instruments, 78, 011302
Girardi, L., et al. 2005, A&A, 436, 895
Gordon, K. D., et al. 2014, ApJ, Submitted
Gordon, K. D., et al. 2011, AJ, 142, 102
Groenewegen, M. A. T. 2006, A&A, 448, 181
Groenewegen, M. A. T. & de Jong, T. 1993, A&A, 267, 410
Groenewegen, M. A. T., et al. 2009, A&A, 506, 1277
—. 2007, MNRAS, 376, 313
Gruendl, R. A., et al. 2008, ApJ, 688, L9
Jackson, D. C., et al. 2007a, ApJ, 656, 818
—. 2007b, ApJ, 667, 891
Jones, A. P. & Nuth, J. A. 2011, A&A, 530, A44
Karakas, A. & Lattanzio, J. C. 2007, PASA, 24, 103
Kastner, J. H., et al. 2006, ApJ, 638, L29
Kim, M., et al. 2009, ApJ, 703, 816
Le Bertre, T. 1992, A&AS, 94, 377
—. 1993, A&AS, 97, 729

Lee, H., et al. 2006, ApJ, 647, 970
Marigo, P., et al. 2013, MNRAS, 434, 488
—. 2008, A&A, 482, 883
Martin, N. F., et al. 2009, ApJ, 705, 758
Mateo, M. L. 1998, ARA&A, 36, 435
Matsuura, M., et al. 2009, MNRAS, 396, 918
Mattsson, L., et al. 2008, A&A, 484, L5
Mayer, L., et al. 2001, ApJ, 547, L123
—. 2006, MNRAS, 369, 1021
McConnachie, A. W. 2012, AJ, 144, 4
McConnachie, A. W., et al. 2005, MNRAS, 356, 979
McDonald, I., et al. 2011a, ApJS, 193, 23
—. 2011b, MNRAS, 417, 20
McQuinn, K. B. W., et al. 2007, ApJ, 664, 850
Meixner, M., et al. 2006, AJ, 132, 2268
Menzies, J., et al. 2008, MNRAS, 385, 1045
Miller, B. W., et al. 2001, ApJ, 562, 713
Moffat, A. F. J. 1969, A&A, 3, 455
Pimbblet, K. A. & Couch, W. J. 2012, MNRAS, 419, 1153
Reach, W. T., et al. 2005, PASP, 117, 978
Riebel, D., et al. 2012, ApJ, 753, 71
Sand, D. J., et al. 2012, ApJ, 756, 79
Schneider, R., et al. 2014, MNRAS, 442, 1440
Sewiło, M., et al. 2013, ApJ, 778, 15
Skillman, E. D., Côté, S., & Miller, B. W. 2003, AJ, 125, 593
Skillman, E. D., et al. 2014, ApJ, 786, 44

Sloan, G. C., et al. 2008, ApJ, 686, 1056
—. 2010, ApJ, 719, 1274
—. 2012, ApJ, 752, 140
Smith, N. 2014, ARAA, 52
Smith, N., et al. 2003, AJ, 125, 1458
—. 2007, ApJ, 666, 1116
Srinivasan, S., et al. 2009, AJ, 137, 4810
Stetson, P. B. 1987, PASP, 99, 191
Tammann, G. A., Reindl, B., & Sandage, A. 2011, A&A, 531, A134
Tosi, M. 2003, Ap&SS, 284, 651
van den Bergh, S. 1999, ApJ, 517, L97
van Loon, J. Th., et al. 2008, A&A, 487, 1055
Vijh, U. P., et al. 2009, AJ, 137, 3139
Voors, R. H. M., et al. 2000, A&A, 356, 501
Wachter, A., et al. 2008, A&A, 486, 497
Watkins, L. L., Evans, N. W., & van de Ven, G. 2013, MNRAS, 430, 971
Weisz, D. R., et al. 2011, ApJ, 739, 5
—. 2014, ApJ, 789, 147
—. 2012, ApJ, 748, 88
Werner, M. W., et al. 2004, ApJS, 154, 1
Wright, E. L., et al. 2010, AJ, 140, 1868
Zhukovska, S. & Henning, T. 2013, A&A, 555, A99

APPENDIX

A. COLOR-MAGNITUDE DIAGRAMS

Figures A1 and A2 show the DUSTiNGS color-magnitude diagrams. We show the combined epochs to demonstrate the maximum photometric depth. The dark shaded regions mark the range of the expected TRGB for each galaxy. The majority of TP-AGB stars are brighter than this limit. The light shaded regions mark the approximate location of x-AGB stars.

B. IMAGES

Figures B1 and B2 show the 3.6 μm epoch 1 mosaics for a subset of the DUSTiNGS galaxies. Galaxies not shown are low mass and have few sources above the TRGB. For these galaxies, it is difficult to see the galaxy among the background and foreground sources. We include Cetus as an example of a low-mass galaxy. See Figure 2 for an example of the imaging strategy.
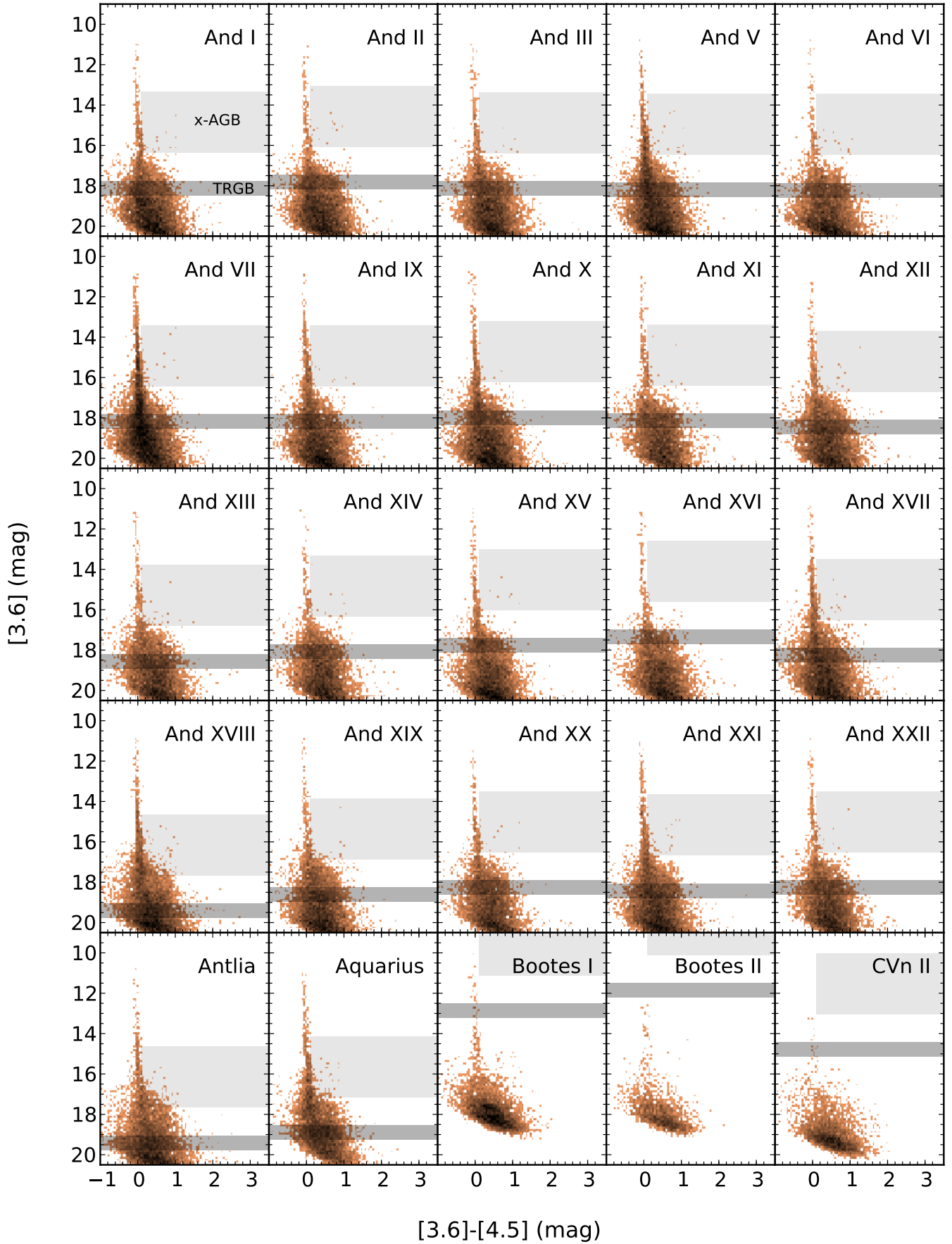
Figure A1. Color-magnitude diagrams of the GSC for each DUSTiNGS galaxy. Magnitudes shown here are derived from the two combined epochs. The dark shaded region marks the range of the possible TRGB and the light shaded region marks the approximate location of x-AGB stars.
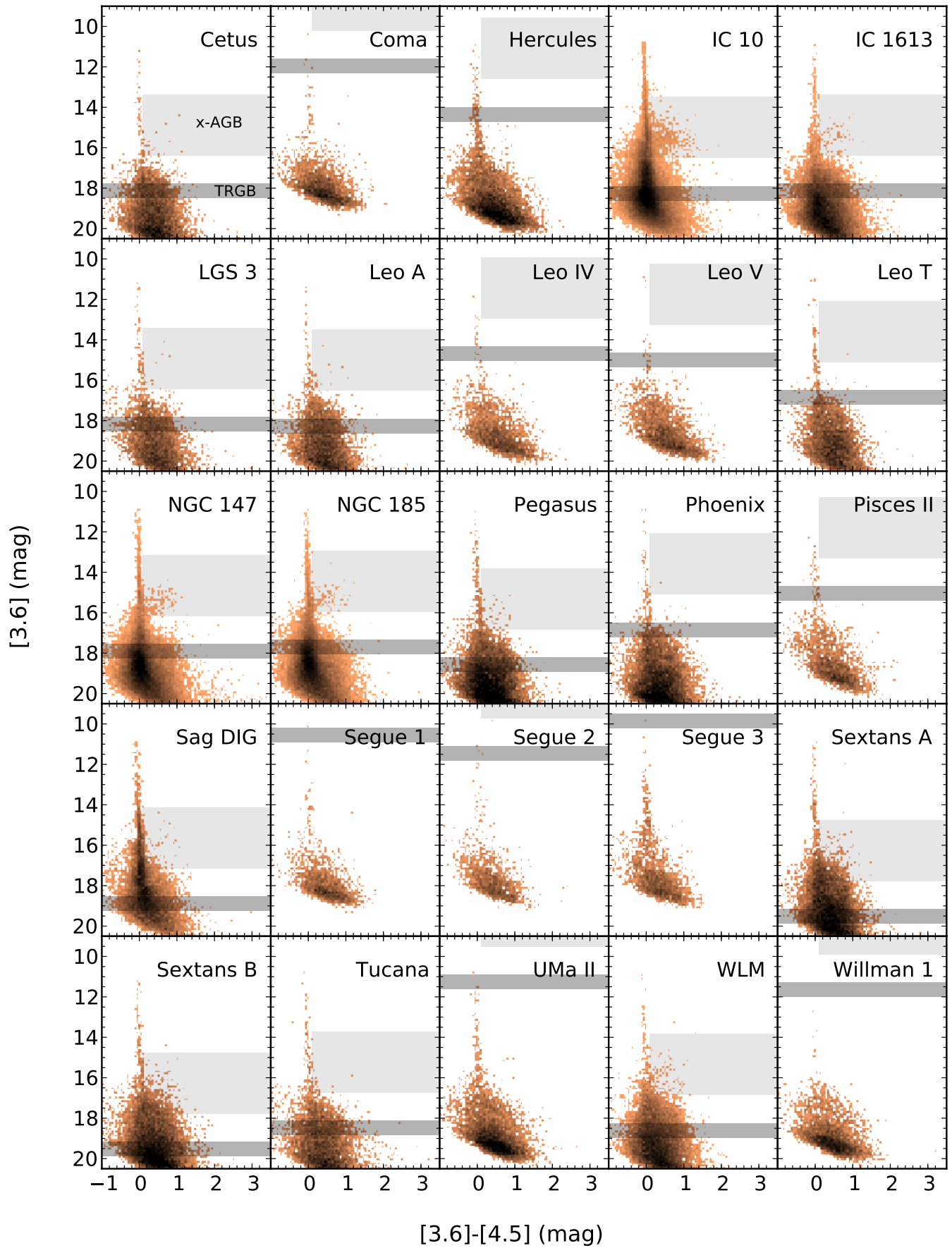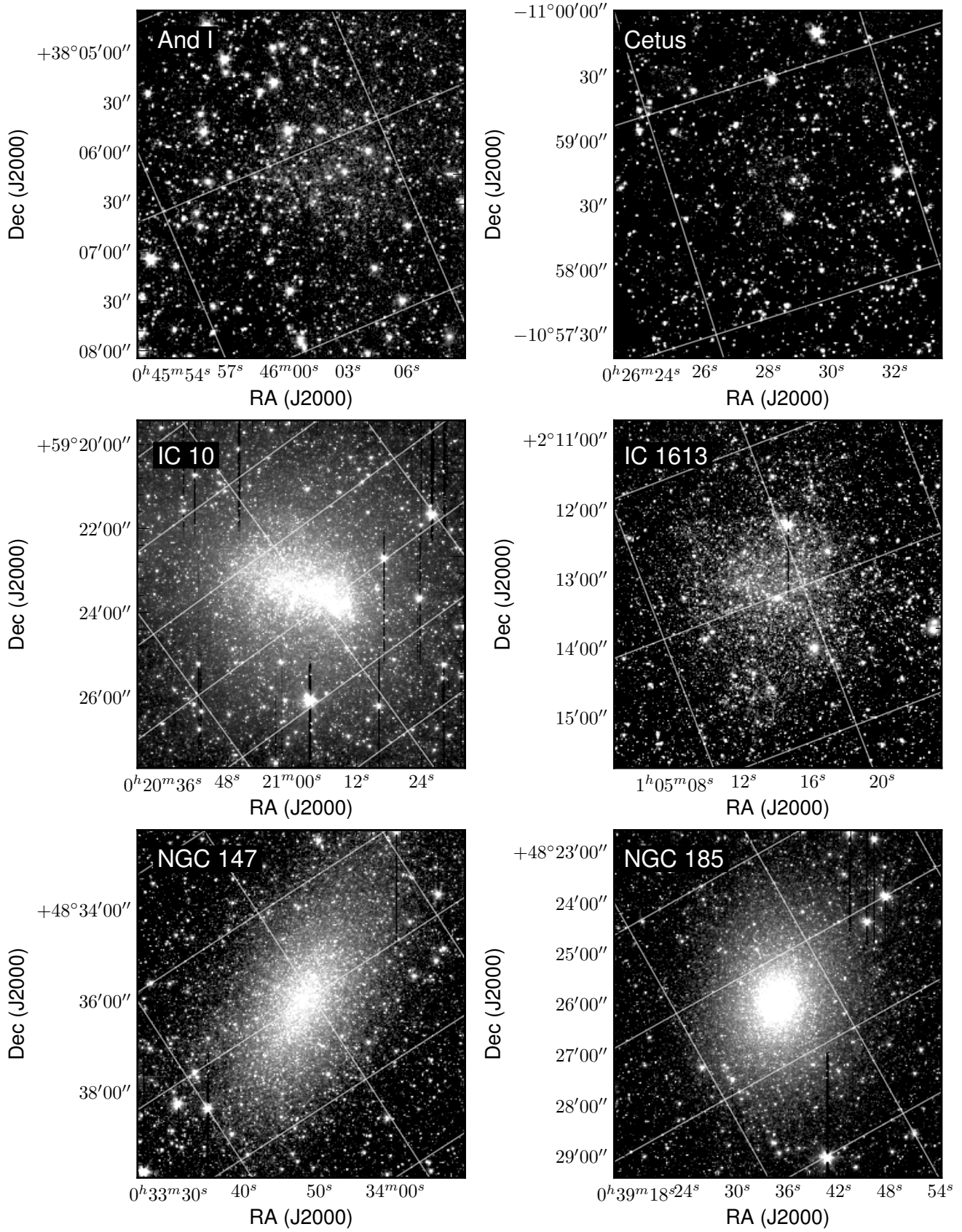
Boyer et al.

Figure A2. Continued.

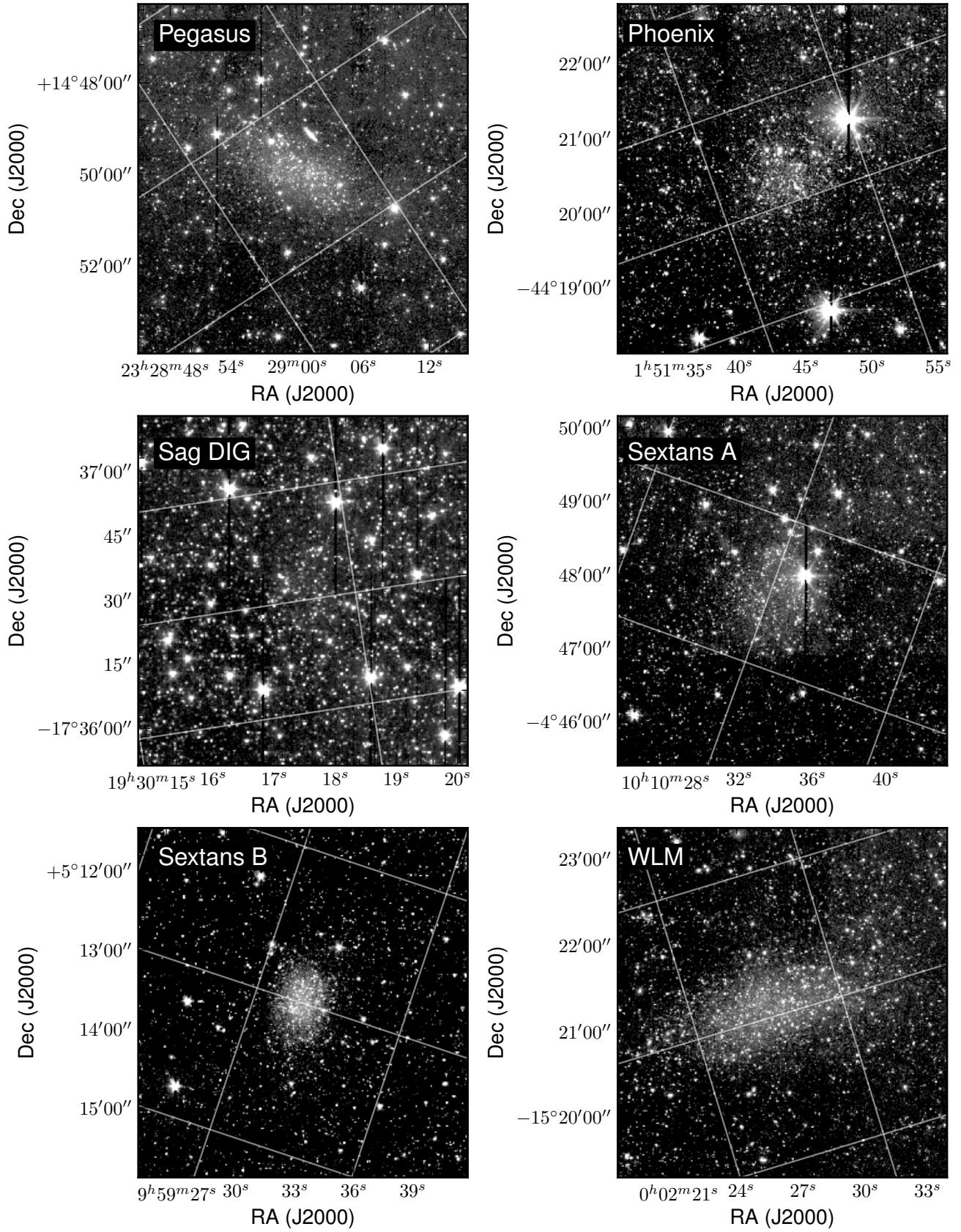**Figure B1.** 3.6 μm epoch 1 mosaics for a subset of the DUSTiNGS galaxies.

Figure B2. Figure B1 continued.